Theories for photoinduced structural phase transitions

AUTHOR(S):

Nasu, Keiichiro

CITATION:

Nasu, Keiichiro. Theories for photoinduced structural phase transitions. 物性研究 2006, 85(6): 764-821

ISSUE DATE:

2006-03-20

URL:

http://hdl.handle.net/2433/110412

Theories for photoinduced structural phase transitions

Keiichiro Nasu

Solid State Theory Division, Institute of Materials Structure Science, KEK,
Graduate University for Advanced Study, 1-1, Oho, Tsukuba, Ibaraki, 〒305-0801, Japan

E-mail: knasu@post.kek.jp

Abstract

本稿では、光誘起構造相転移に関する理論的研究の現状を、遍歴電子モデルを中心にして、随時、実験とも関連させながら紹介する。基本となる概念は、固体結晶に潜在する多重安定性である。フェルミ面の極く近傍のみを観測する種々の熱力学的測定では、殆ど明瞭に観測されない場合でも、対象となる固体結晶が、潜在的に多重安定性を有する事が様々に予想され、これは、僅かな光励起で非平衡相転移となって実際に観測される。有機電荷移動型錯体結晶、有機金属錯体、ペロブスカイト型誘電体、等々を具体例として、この種の研究を通覧する。

Theories for photoinduced structural phase transitions are reviewed in close connection with various recent experimental results related to this new optical phenomenon. There are two key concepts: the hidden multi-stability of the ground state, and the proliferations of optically excited states. Taking the ionic(I) → neutral(N) phase transition in the organic charge transfer(CT) crystal, TTF-CA, as a typical example for this type transition, we, at first, theoretically show an adiabatic path which starts from CT excitons in the I-phase, but finally reaches to a N-domain with a macroscopic size. In connection with this I-N transition, the concept of the initial condition sensitivity is also developed so as to clarify experimentally observed nonlinear characteristics of this material.

In the next, using a more simplified model for the many-exciton system, we theoretically study the early time quantum dynamics of the exciton proliferation, which finally results in the formation of a domain with a large number of excitons. For this purpose, we derive a stepwise iterative equation to describe the exciton proliferation, and clarify the origin of the initial condition sensitivity.

Possible differences between a photoinduced nonequilibrium phase and an equilibrium phase at high temperatures are also clarified from general and conceptional points of view, in connection with recent experiments on the photoinduced phase transition in an organo-metallic complex crystal. It will be shown that the photoinduce phase can make a new interaction appear as a broken symmetry only in this phase, even when this interaction is almost completely hidden in all the equilibrium phases, such as the ground state and other high-temperature phases. The relation between the photoinduced nonequilibrium phase and the hysteresis induced nonequilibrium one is also qualitatively discussed.

We will be concerned with a macroscopic parity violation and a ferro- (or super-para-) electricity, induced by a photogenerated electrons in the perovskite type quantum dielectric $SrTiO_3$. The photogenerated electron in the 3d band of Ti, is assumed to couple, weakly but quadratically with soft-anharmonic T_{1u} phonons, and strongly but linearly to the breathing (A_{1g}) type high energy phonons. These two types of electron-phonon couplings result in two types of polarons, a "super-para-electric large polaron" with a quasi-global parity violation, and an "off-center type self-trapped polaron" with only a local parity violation. This super-para-electric large polaron, being equal to a charged and conductive ferroelectric domain, greatly enhances both the quasi-static electric susceptibility and the electronic conductivity.

We also briefly review recent successes to observe the photoinduced structural phase transitions more

directly by using x-ray measurements.

Contents

1. Equilibrium phases, nonequilibrium phases and photoinduced phase transitions

Large varieties of materials are now around us. These materials are such ones, that few kinds of macroscopic numbers of atoms or molecules are condensed with a definite composition ratio. While, without changing this chemical composition, a material can take various phases from gaseous and liquid phases to crystalline ones, as temperature decreases from high to low. Even at low temperatures, a material can take various crystalline phases, whose lattice structure and electronic state change as temperature decreases. However, all these states are so-called equilibrium phases, in the sense that the free energy of each state takes its global minimum at each temperature.

Let us now proceed to nonequilibrium phases generated from an equilibrium one by some external excitations or stimulations. Usually, these states are transient ones having higher energies than the equilibrium one, but, depending on the way of the stimulations or excitations, we can get much more varieties of states, even if the starting equilibrium phase is same. They also surely relax down to the starting equilibrium one after a period of time. However, if they are locally stable state, in the sense that their free energies take local minima separated from the global one by substantial energy barriers, the time required for the relaxation will be long. In that case, we can complete necessary observations to determine their characteristics within this period of time. Hence, such a long-lived locally stable nonequilibrium phase is effectively same as the equilibrium ones.

Various amorphous crystals are well known as typical examples for these nonequilibrium phases. They are brought about by cooling materials down rapidly from their high temperature phases. The lifetime of the relaxation is believed to be much longer than the time scale of our daily life. Unfortunately, however, these amorphous crystals have no well-defined long range periodic crystalline or electronic order, since they are just amorphous.

Very recently, on the other hand, there discovered a new class of insulating solids, which, being shone by only a few visible photons, become pregnant with a macroscopic excited domain that has new structural and electronic orders quite different from the starting ground state (equilibrium phase). This phenomenon is called “photoinduced phase transition” and we can generate new long lived locally stable macroscopic nonequilibrium phases through the excitations or stimulations by a few visible photons. The purpose of this paper is to review recent theoretical studies on this phenomenon, in close connection with various recent experiments.

2. Relaxation of optical excitations, hidden multi-stability and photoinduced phase transitions

As is already well known, an electron in an insulating crystal induces a local lattice distortion around itself, when it is excited by a photon. A sudden change of charge distribution appeared through this optical excitation, induces a motion of the crystal lattice surrounding the excited electron, so that the whole electron-lattice system will reach a new equilibrium position within the excited state. This phenomenon is called “lattice relaxation” of an optical excitation, and the resultant state is often called “photoinduced structural change”, as schematically shown in Fig.1. This relaxation phenomenon has been studied in detail, in various kinds of insulating crystals for these fifty years. According to the original concept of this lattice relaxation, however, it is tacitly assumed to be a microscopic phenomenon, in which only few atoms and electrons are involved[1].

In the recent years, on the other hand, there have been discovered many unconventionally photoactive solids, where the relaxation of optical excited states results in various collective motions involving a large number of atoms and electrons. In some cases, it results in a macroscopic excited domain with new structural and electronic orders quite different from the original ones. This situation can be called "photoinduced structural phase transition (PSPT)"[2-5].

These problems are closely related with the hidden multi-stability intrinsic to each solid. If the ground state of a solid is pseudo-degenerate, being composed of true and false ground states with each structural and electronic orders different from others, we call it multi-stable. In this case, the photo-absorption, being initially a single-electron excitation from the true ground state, can trigger local but

macroscopic instabilities. The photo-absorption can induce low-lying collective excitations during the lattice relaxation, and can finally produce a false ground state at the expense to create boundaries between the two states. Thus a local but macroscopic excited domain appears. In other words, the initially created single-electron excitation proliferates during the relaxation, and grows up to be a macroscopic order, as schematically shown in Fig.1.

The origin of the pseudo-degeneracy can be understood from the conceptional point of view related with the cohesive mechanism of each solid. As mentioned before, the solid is composed of macroscopic numbers of few kinds of atoms or molecules with a definite composition ratio. However, even if the constituent atoms (molecules) are defined, the structural and electronic orders, which will be realized in the macroscopic ground state, are not always determined straightforwardly. For example, in the case of alkali halide, the ionic state and the covalent one are two well-known candidates for the ground state[6]. Moreover, if there are two predominant but mutually conflicting elements in the original Hamiltonian, there appear two candidates that inherit this conflict. Thus, it is quite ubiquitous that we have the multi-stability or the pseudo-degeneracy with the true and false ground states.

It is also very important to see the relation between photoinduced phase transitions and the ordinary ones due to the thermal excitation. When the false ground state is so fortunate to be just above the true one, being easily excited by the thermal energy, we may get the ordinary phase transition, and can recognize the presence of this false ground state. However, there will be various other cases that the energy of the false ground state is too high to be excited thermally. Ordinary thermodynamic measurements can be concerned only with the true ground state or small excitations therefrom, and hence, they can never detect such hidden states. Even in these difficult cases, we can create the false ground state by the photo-excitation and the lattice relaxation therefrom, as schematically shown in Fig.1.

Such a false ground state always disappears finally within a finite life-time, and can never be permanent, as mentioned before. However, according to the recent progress of our laser spectroscopy techniques, an infinite life time is no more necessary for each state to be recognized as a well-defined state, provided that can last long enough to be clearly observed by other photons to detect it. At present, the time required for this type observation is usually less than 10^{-12} second, and in some case, even 10^{-15} second is enough.

Incidentally, let us briefly see, the difference between the present photoinduced phase transition and the so-called "new material design (or search)", which is the most contemporary trend in the field of the material science. The one of most standard techniques for the new material design (or search) is to apply static external fields such as magnetic fields or pressures onto a material, which is expected to give novel or anomalous properties absent in other materials existing already. The other most standard technique is to design or synthesize the material by changing its chemical composition, little by little, so that it will show quite new properties.

In the case of static external field, however, it changes all the electronic state of the material, both ground and excited states, unselectively. While photons have definite momentum, phase, helicity and energy. Hence, they can create only particular excited states, selectively and quite intensively. In contrast to the chemical design or synthesis, the photoinduced phase transition does not change the chemical composition of the material, but can realize new states. Thus the research for photoinduced phase transitions will be able to open a new multistoried concept for materials.

3. Photoinduced ionic → neutral phase transition in organic molecular crystal TTF-CA

As one of the typical examples for the PSPT, here, we will be concerned with the photoinduced ionic(I)→ neutral(N) transition in an organic molecular crystal Tetrathiafuluvalene-p-Chloranil, and review the present stage for its experimental studies. Both Tetrathiafuluvalene (TTF) and p-Chloranil (CA) are planar organic molecules as schematically shown at the top of Fig.2, and their crystal has a quasi 1-d chain like structure, in which these two molecules are alternately stacked along this 1-d chain axis.

In the true ground state of this crystal at absolute zero of temperature, both TTF and CA become a cation and an anion, respectively, and make a dimer with each other as shown in Fig.2a. This is called the I-phase. On the other hand, we also have the N-phase, in which neutral TTF and CA are stacked alternately without dimerization, as shown in Fig.2d. This is the accidentally pseudo-degenerate false ground state, and at absolute zero of temperature, it is just above the ionic true ground state.

Keeping this material in the low enough temperature, but shining a strong laser light of about 0.6eV~2.3eV on to it, we can generate the N-domain even in the ionic true ground state, as shown in Fig.2c. This change was experimentally confirmed by the change ($\equiv \Delta R$) of the optical reflectivity. Figure 3 shows the spectral shape of original optical reflectivity ($\equiv R$) of the TTF-CA crystal in the I-phase at 2K, where the exciting light is polarized perpendicular to the 1-d chain axis[7]. In this spectrum, we can see a characteristic peak structure at around 3eV, and this peak corresponds to an intra-molecular electronic excitation of TTF^+. Hence its intensity can be used as a macroscopic indicator for the presence of the cationic TTF molecules in this crystal.

In fact, when this crystal is shone by a light with an energy of 2.3eV, we can get a relative change ($\equiv \Delta R/R$) of this reflectivity, as shown in Fig.4[8]. The intensity of the aforementioned peak is clearly seen to decrease. It means that a macroscopic number of neutral TTF molecules (N-domains) have been generated in the I-phase. This is nothing else but the PSPT. From this decrease of the peak intensity, we can determine that the domain is composed of about 200~1000 neutral pairs, and it can last for about 10^{-3} second[8].

4. Threshold excitation intensity and initial condition sensitivity

For this transition, we can think of the following simple and intuitive scenario as schematically shown from Fig.2b to Fig.2c. That is, a single photon can make a single charge transfer (CT) excitation between neighboring molecules, which is just equal to a neutral pair generation. After that, the number of this neutral pair will increase like a domino game. However, by the recent experimental studies shown in Fig.5[9], this simple scenario is proved wrong.

In this figure, we have shown the photo-absorption spectrum of TTF-CA, as a small inset. It has two peaks at 0.6eV and also at 2.2eV. The first one, being the elementary optical excitation of this crystal, corresponds to the aforementioned inter-molecular CT excitation. Among a macroscopic number of neighboring ion pairs (TTF^+ and CA^-) in Fig.2a, only a single neighboring ion pair returns back to a neutral pair (TTF and CA) by this excitation as shown in Fig.2b, and this neutral pair also itinerates along the crystal axis, keeping all other pairs still ionic. This is nothing else but the so-called inter-molecular CT exciton, wherein a hole and an electron (a positive charge and a negative one relative to the I-phase) are bound together, so that they are always at neighboring two molecules with each other, even if their center of mass itinerates. While, the second peak at 2.2eV corresponds to an intra-molecular electronic transition of TTF, just like the case of the aforementioned 3eV peak. The thick solid line in Fig.5 denotes the efficiency of the N-phase generation as function of the exciting photon intensity, when the photon energy is fixed at this CT exciton (0.6eV). We can clearly see that there is a threshold in the intensity, below which the macroscopic N-phase can never be generated. It means that a single CT exciton alone can never result in the macroscopic N-phase, but only through a nonlinear cooperation between several photo-excited CT excitons, the new phase can be attained. The presence of this threshold is the first note-worthy characteristic of the TTF-CA crystal.

The second note-worthy characteristic, which we can see from Fig.5, is the difference between the

dashed line and the aforementioned thick solid line. Exactly speaking, the horizontal axis of this figure does not simply denote the photon intensity itself, but denotes the total photon energy which is absorbed in the unit volume of the TTF-CA crystal. This total energy is calculated by taking the three quantities into account, the absorption coefficient, the energy of the photon and its intensity. Thus, we can compare the 0.6eV excitation and the 2.2eV excitation (the thick dashed line) on an equal footing. For example, if we focus on the point with a value 0.25 of the horizontal axis in Fig.5, we can find that the efficiency becomes very high or almost zero, depending sensitively on the photon energy, although the total absorbed photonic energies are same each other. Not only these two cases, we can also excite using various other photons in between (0.6eV~2.2eV), keeping the total absorbed photonic energies are same. However all these excitations give the efficiencies different with each other, and ranging between the two lines in Fig.5.

From this fact, we can immediately conclude that it is not the ordinary thermal phase transition. In the experimental studies for photoinduced phase transitions, the first thing we have to examine is, whether it is the ordinary thermal phase transition or not. Because, the absorbed photons may often be converted into heat in the crystal, raising up its temperature, and may indirectly result in the ordinary thermal phase transitions. In the case of this indirect thermal phase transition, however, its generation efficiency will depend only on the total absorbed photon energy, and will never sensitively depend on the way or type of the excitation. While, Fig.5 shows that the generation efficiency quite sensitively depends on the type of the excitation, that is, the exciting photon energy, even if the total absorbed photonic energies are same. If we return back to Fig.1, the aforementioned two types of excitations start from the common ground state minimum equally, and moreover, the energies of the final states of the Franck-Condon transition are almost same.

Here, we should emphasize the so-called Franck-Condon principle. The optical transition can complete within a time of the order of 10^{-15} second, provided that its transition energy is in the visible region. While, the period of oscillation of a crystal lattice or phonon is of the order of 10^{-12} second. Thus, the configuration of the crystal lattice can never change during the optical transition, and hence, it can occur only vertically as schematically shown in Fig.1. Consequently, possible differences between the aforementioned two transitions are only in the electronic natures of these Franck-Condon type excited states, from which the lattice relaxation and the proliferation start. However, this small difference in the initial state of the relaxation, afterwards diverges and finally determines occurrence or nonoccurrence of the photoinduced phase transition. This is the so-called "initial condition sensitivity", peculiar to the dynamics of nonlinear systems.

As is well known, the initial condition sensitivity has been studied mainly from the mathematical point of view, by taking classical nonlinear model systems with only a few degree of freedoms[10]. The setting up the initial condition, in this case, is also purely mathematical and artificial procedure in order to solve nonlinear differential equations that describe these model systems. On the other hand, the present case is the formation of a macroscopic order in a real material, and the setting up the initial condition itself is also a real physical process. As mentioned before, it is set by choosing the spatiotemporal pattern of the exciting photon pulse, and hence, it is in compliance with the quantum uncertainty. Thus the studies for the photoinduced phase transitions will open new aspects of the nonlinear dynamics and self-organization phenomena.

5. Adiabatic path of photoinduced ionic → neutral phase transition in TTF-CA crystal

Keeping these points in mind, very recently, Huai et al have theoretically clarified the adiabatic relaxation path, which starts from a Franck-Condon type optical excitation in the ionic ground state of the TTF-CA crystal, and terminates up to the large N-domain formation in this crystal[11]. Let us review it in detail. In order to clarify the photoinduced phenomena in TTF-CA theoretically, we have to specify our microscopic model to describe the many-electron system strongly coupling with lattice distortions (phonons) in this molecular crystal. The constituent TTF and CA molecules are, of course, originally neutral. However, when

they are condensed as a crystal at low enough temperatures below 84K, the whole system becomes the ionic and dimerized phase shown in Fig.2(a). While, at higher temperatures than 84K, it returns back to the neutral and monomeric phase as shown in Fig.2(d), and this ordinary thermal phase transition is the first order one[12].

As shown by Soos theoretically[13], the change from the original neutral state to the ionic one in TTF-CA can be described as an electron transfer from the highest occupied molecular orbital (HOMO) of TTF to the lowest unoccupied molecular orbital (LUMO) of CA. The main energy gain in the ionic state relative to the neutral one is the long range Coulomb interaction between electrons and ions, in particular, the Coulomb attraction between a cation and an anion thus generated, and this energy gain increases if the inter-molecular distance decreases after the ionization, as firstly shown by Sakano-Toyozawa[14].

5.1 Model Hamiltonian

Theory by Huai et al[11] is intended to take these essential points into account straightly, and based on the extended Peierls-Hubbard model for valence electrons in the HOMO of TTF molecules and the LUMO of CA molecules as schematically shown in Fig.6. The inter-molecular Coulomb repulsion in this model is assumed to depend nonlinearly on the inter-molecular distance. This model also takes weak interactions between 1-d chains into account, so that we can describe the N-domain formation in the three dimensional TTF-CA crystal more realistic. Our Hamiltonian ($\equiv$H) reads,

$$H = H_{el} + H_{ph} + H_{inter}, \qquad (1)$$

where H_{el} , H_{ph} and H_{inter} denote the Hamiltonians of the electron part, the phonon part and the inter-chain interaction. The electronic part H_{el} is given as

$$H_{el} \equiv -T_i \sum_{\ell,\sigma}\left[\left(C^{+}_{\ell,\sigma}C_{\ell+1,\sigma}\right)+(\text{h.c.})\right]+\frac{\Delta}{2}\sum_{\ell}(-1)^{\ell}\, n_{\ell}+U\sum_{\ell} n_{\ell,\alpha}n_{\ell,\beta}$$

$$-\sum_{\ell\in\text{odd}} V_{\ell}(q_{\ell},q_{\ell+1})[2-n_{\ell}]n_{\ell+1}-\sum_{\ell\in\text{even}} V_{\ell}(q_{\ell},q_{\ell+1})[2-n_{\ell+1}]n_{\ell}, \qquad (2)$$

$$n_{\ell,\sigma} \equiv C^{+}_{\ell,\sigma}C_{\ell,\sigma}, \quad n_{\ell} \equiv \sum_{\sigma} n_{\ell,\sigma}, \qquad (3)$$

where T_i is the transfer energy of an electron between a HOMO and its neighboring LUMO. $C^{+}_{\ell,\sigma}$ is the creation operator of an electron with spin $\sigma(=\alpha,\beta)$ at ℓ th lattice site, which is numbered from left to right along the 1-d chain as shown in Fig.6, and odd sites correspond to the HOMO, while the even ones correspond to the LUMO. Δ in eq.(2) is the energy difference between the HOMO and the LUMO, while U is the intra-molecular Coulomb repulsive energy of electrons, and is assumed common to both the HOMO and the LUMO. V_{ℓ} in the second line of eq.(2) is the Coulomb interaction between neighboring two molecules, wherein the total charge in the TTF site ($\ell\in$odd) is +[2-n_{ℓ}], while that in the CA site ($\ell\in$even) is -n_{ℓ}. As mentioned before, this interaction is assumed to depend nonlinearly on the change of the inter-molecular distance $(q_{\ell}-q_{\ell+1})$, where q_{ℓ} is the displacement of each molecule along the chain

axis as shown in Fig.6. The unit of length is the original inter-molecular distance. Thus, V_ℓ is given as

$$V_\ell(q_\ell, q_{\ell+1}) = V_0 + \beta_1(q_\ell - q_{\ell+1}) + \beta_2(q_\ell - q_{\ell+1})^2, \qquad (4)$$

where V_0 is the original value of V_ℓ, while β_1 and β_2 are its first and second order expanding coefficients with respect to $(q_\ell - q_{\ell+1})$.

It is well known that the electron-phonon coupling leading to the dimerization may have two origins. The first one is the present case shown in eq.(4), being the modulation of V_ℓ, and this model is proposed firstly by Sakano-Toyozawa[14]. While, the second one is the modulation of T_i [15-17]. Our model is not this second one. Because of the small overlap between the HOMO and the LUMO, this T_i becomes so small, that its distance variation can be neglected. Moreover, as we will show later in detail, our model is rather straightforward to make the N-I phase transition to be the first order one, in contrast to the SSH model[15], which makes the transition to be the second order.

The phonon part H_{ph} of eq.(1) is given as,

$$H_{ph} \equiv \sum_\ell \frac{S_1}{2}(q_\ell - q_{\ell+1})^2 + \sum_\ell \frac{S_2}{4}(q_\ell - q_{\ell+1})^4, \qquad (5)$$

wherein a fourth order potential with a coefficient S_2 is introduced, as well as the ordinary second order one with the coefficient S_1, while the kinetic energy of phonons are neglected because of the adiabatic approximation.

As for the inter-chain interaction H_{inter}, we neglect it in the study for the ground state properties. This inter-chain interaction is tacitly assumed to be so small as to give almost no contribution provided that the ground state is uniform for all over the chains in the crystal, no matter what it will be the dimerized I-phase or the monomeric neutral one. Only if a large and macroscopic domain appears in the I-phase, this inter-chain interaction is assumed to bring an appreciable energy increase. We will give its practical form later in detail.

Using this model Hamiltonian, let us now set up our simple-minded picture for both the I- and N-phases. The N-phase is such that the HOMO of the TTF is filled up with two electrons of opposite spins ($\uparrow$ and $\downarrow$), while the LUMO of the CA is vacant, as schematically shown in Fig.6(a). Thus, the two constituent molecules are literally neutral, while, the electronic state realized in this system is just equal to the charge density wave (CDW) state of the double period. On the other hand, the I-phase is such that the HOMO and the LUMO are alternately occupied by the electrons of $\uparrow$ and $\downarrow$ spins as shown in Fig.6(b). Within this simple-minded picture, this state is just equal to the spin density wave (SDW) state of the double period. However, as shown in Fig.6(b), this I-phase also has the dimerization between neighboring TTF and CA molecules.

Here we should note why eq.(4) is nonlinear and eq. (5) is anharmonic. If we retain only the linear term in eq.(4), the energy gain due to the dimerization in the I-phase cancels between left and right of each

molecule, since our system is not a single ionic pair but a 1-d chain crystal. For this reason, the nonlinear term is introduced in eq.(4). Accordingly, the quartic anharmonicity is also introduced in eq.(5). It comes from the inter-molecular repulsion, and prevents unphysically large dimerizations.

In our theory, we have eight parameters $T_i, \Delta, U, V_0, \beta_1, \beta_2, S_1$ and S_2. The values of these parameters are determined so that, they, as a set, reproduce main experimental and theoretical results existing already prior to our theory. For T_i, we use the ab-initio calculation by Katan[18]. On the other hand, from spectroscopic studies in the visible and infrared regions, the total charge induced at the CA site of the I-phase ($\equiv \rho_I$) is determined to be $\rho_I = 0.8$ [19]. While, by the same experiment, the total charge induced at the CA site of the N-phase ($\equiv \rho_N$) is also determined as $\rho_N = 0.3$. Unlike the simple-minded picture shown in Fig.6, these induced charges ρ_I and ρ_N are not natural numbers such as 1 or 0, but are fractional, because the valence electrons are quantum-mechanically itinerant, or T_i is not zero. In addition to these, there are following five well-known experimental results. By the x-ray structure analysis, the dimeric displacement of each molecule in the ionic ground state is determined to be 2.5% of the original intermolecular distance[12]. More over, in the light absorption spectrum of the I- phase, two CT absorption peaks appear at 0.6eV and 1.0eV with an intensity ratio 1: 0.5, while, in the N-phase, only a single CT peak appears at 0.6eV[19]. Using these data, we can determine our eight parameters without serious ambiguity as, T_i =0.17eV, Δ =2.716eV, U= 1.528eV, V_0 =0.604eV, β_1 =1.0eV, β_2 =8.54eV, S_1 = 4.86eV and $S_2 = 3.4\times10^3$ eV.

5.2 Ground state properties

Let us now see the properties of the ground state given by this Hamiltonian H, using. the unrestricted Hartree-Fock approximation. Within this approximation, we can reduce the two-body terms of H_{el} into one-body terms as

$$U n_{\ell,\alpha} n_{\ell,\beta} \rightarrow U\left(n_{\ell,\alpha}\langle n_{\ell,\beta}\rangle + \langle n_{\ell,\alpha}\rangle n_{\ell,\beta} - \langle n_{\ell,\alpha}\rangle\langle n_{\ell,\beta}\rangle\right), \qquad (6)$$

$$V_\ell\, n_\ell\, n_{\ell+1} \rightarrow$$

$$V_\ell\left\{\left(n_\ell\langle n_{\ell+1}\rangle + \langle n_\ell\rangle n_{\ell+1} - \langle n_\ell\rangle\langle n_{\ell+1}\rangle\right) - \sum_\sigma\left(\langle m^+_{\ell,\sigma}\rangle m_{\ell,\sigma} + m^+_{\ell,\sigma}\langle m_{\ell,\sigma}\rangle - \langle m^+_{\ell,\sigma}\rangle\langle m_{\ell,\sigma}\rangle\right)\right\}, \qquad (7)$$

$$m_{\ell,\sigma} \equiv C^+_{\ell,\sigma} C_{\ell+1,\sigma}, \qquad (8)$$

where $\langle\cdots\rangle$ denotes the expectation value of an operator $\cdots$. It is unknown at present stage, but will be determined later self-consistently. Since our system is the half-filled system wherein the total number of

the lattice sites ($\equiv N_t$) is equal to the total number of electrons as

$$\frac{N_t}{2} = \sum_{\ell} n_{\ell,\alpha} = \sum_{\ell} n_{\ell,\beta}\,, \qquad (9)$$

we assume for $\langle n_{\ell,\sigma}\rangle$, $\langle m_{\ell,\sigma}\rangle$ and q_ℓ the following forms with the double period,

$$\langle n_{\ell,\sigma}\rangle = \frac{1}{2} + (-1)^{\ell}\delta n_{\sigma}, \quad \langle m_{\ell,\sigma}\rangle = \overline{m}_{\sigma} + (-1)^{\ell}\delta m_{\sigma}, \quad q_\ell = (-1)^{\ell}\, q_0, \qquad (10)$$

where δn_σ, $\overline{m}_\sigma$, δm_σ and q_0 are to be determined within the Hartree-Fock and adiabatic approximations.

The Hartree-Fock type self-consistent equation for these δn_σ, $\overline{m}_\sigma$ and δm_σ gives two solutions for a given q_0, and they correspond to the I-phase with $\delta n_\alpha \approx -\delta n_\beta$ (SDW) and to the N-phase with $\delta n_\alpha \approx \delta n_\beta$ (CDW). In Fig.7, we have shown the total energy ($\equiv E_g$) thus theoretically calculated as a function of q_0, and these I- and N-phases are shown to be pseudo-degenerate with each other[11]. The energy minimum of the I-phase is 0.002eV lower that of the N-one, and they are separated by an adiabatic energy barrier of about 0.0045eV. Thus the I-phase is the true ground state, while the N-phase is the false one, and both these two phases are locally stable. Furthermore, the I-phase is theoretically shown to be dimerized about 2.9% of the lattice constant, while the N-phase is not dimerized ($q_0 = 0$). Although we have been concerned only with the adiabatic energy at absolute zero temperature, the presence of the aforementioned adiabatic energy barrier means that the ordinary thermal phase transition between N-phase and I-one is the first order.

In Fig.8(a), we have illustrated the charge and the spin density distributions calculated for the I-phase. This phase is characterized by the strong SDW order ($\delta n_\alpha \approx -\delta n_\beta \approx 0.4$) mixed with a weak CDW type order. The calculated induce charge ρ_I is 0.95, being quite large but still fractional. Fig.8(b) demonstrates the N-phase, and there is only the CDW type order ($\delta n_\alpha \approx \delta n_\beta \approx 0.4$). The calculated induced charge ρ_N of this phase is 0.2, being comparatively small, but still significant due to the finiteness of T_i.

5.3 Energy band structure and lowest excited state

Fig.9(a) presents four one-electron energy bands of the I-phase, obtained as functions of a wave-vector ($\equiv k$), by using this unrestricted Hartree-Fock approximation. It has an antiferromagnetic broken symmetry in the spin space. There are two bands for each up- and down-spin electrons as distinguished by the corresponding arrows in Fig.9(a). In the ground sate, the lower two bands are occupied, while others are vacant. The lowest band, being occupied by up-spin electrons, is mainly composed by the LUMO of TTF, while the second lowest band, being occupied by down-spin electrons, are mainly composed of the HOMO of CA. In this system, the elementary optical excitation is such that a down-spin electron goes

from the second lowest band to the third one, as shown by a dashed arrow in Fig.9(a). This third band is mainly composed of the HOMO, which is already occupied by an up-spin electron, and hence the excitation energy partly due to U in eq.(2).

If we change our picture from the wave-vector space to the real space, this excitation results in a doubly occupied HOMO and a vacant LUMO, while all other sites still keep original single occupancy. The electron and the hole thus created by light, attract with each other through $-V_\ell$, and make the aforementioned bound state called the CT exciton, as schematically shown in Fig.9(b), and this CT exciton is the same one as already shown in Fig.2(b). This is the lowest Franck-Condon type excited state, calculated by the theory based on the unrestricted Hartree-Fock approximation, reinforced by including the electron-hole attraction at the final state of the optical transition[11].

Using this reinforced theory, Huai et al have calculated the spectral shape of the CT excitation including classical lattice fluctuations[11]. The resultant spectral shape has two peaks at 0.6eV and at 1.0eV in the case of the I-phase, while, in the case of N-phase, it has only a single peak at 0.6eV. This result is consistent with the experimentally observed spectral shape of the light absorption in the energy region from 0.6eV to 1.3eV[19]. The theoretical origin of this change from the two peaked structure to the single peaked one was firstly demonstrated by Sakano-Toyozawa[14], and the present theoretical result is identical to it, if the thermal lattice fluctuations are completely frozen. Thus, the present theory can successfully reproduce various well-known experimental and theoretical results.

5.4 Relaxation path

Let us now proceed to the lattice relaxation path of optical excitations. The visible photon has a long wavelength of about 1000 times of the lattice constant, and each photon can make a single CT exciton per this length. Among many excitons thus created in the whole ionic crystal, we will focus only on a single CT exciton and will clarify its lattice relaxation path. This path starts from the Franck-Condon state, and terminates up to the macroscopic N-domain formation. In order to describe this path theoretically, we introduce the following domain type lattice distortion pattern q_ℓ,

$$q_\ell = (-1)^\ell q_0 \left\{ 1 + \Delta q \left[\tanh\left(\theta \left(|\ell| - \frac{\ell_0}{2} \right) \right) - 1 \right] \right\}. \qquad (11)$$

Here $(-1)^\ell q_0$ denotes the uniform dimeric distortion of the ionic ground state, from which we start. The second term in the curly brackets $\{\cdots\}$ denotes a local lattice displacement induced by a new excited domain. Δq is its amplitude, θ corresponds to the width of the domain boundary, and ℓ_0 is the domain size. Typical domain structures given by these parameters are demonstrated in Fig.10. When $\Delta q < 0.5$, the lattice site ℓ inside of the domain ($-\ell_0/2 \le (\ell - 50) \le \ell_0/2$) has a reduced dimerization, but is still in the same phase as the original lattice outside of the domain, and hence it corresponds to a new I-domain. In the case of second situation $\Delta q = 0.5$, it is obvious that the inside lattice sites have no dimerization at all. Therefore, it corresponds to a N-domain.

Let us return to the problem of H_{inter}. The distance between the TTF and the CA molecules within

a chain is about 3 Å, while the inter-chain distance is about 10 Å, and hence, as mentioned before, we have neglected this interaction, assuming that it will give no serious effect. Even for the excited domain, this situation will be same, if the new displacement $(q_\ell - (-1)^\ell q_0)$ associated with this new domain is small as compared with the original displacement in the ground state, $|q_\ell - (-1)^\ell q_0| \leq q_0$. On the other hand, when the new displacement becomes very large, $|q_\ell - (-1)^\ell q_0| >> q_0$, various inter-molecular repulsions will also act, and will give a nonlinear increase of the lattice potential, just as shown in eq.(5) and Fig.7. Moreover, this effect will become appreciable only when the new domain expands to a macroscopic size in a single chain. To take this nonlinear inter-chain interaction into account effectively, Huai et al used the following form,

$$H_{inter} = \sum_\ell \left\{ K_1 \left(q_\ell - (-1)^\ell q_0 \right)^2 + K_2 \left(q_\ell - (-1)^\ell q_0 \right)^4 + K_3 \left(q_\ell - (-1)^\ell q_0 \right)^6 \right\}, \quad (12)$$

where q_ℓ denotes the lattice distortion of a central chain on which we focus, while $(-1)^\ell q_0$ is the representative of the displacements of environmental chains, and K_i (i=1,2,3) denotes the 2i th expanding coefficient with respect to the new distortion. These environmental chains are assumed to be frozen in the ionic ground state, being never excited whatever occurs in the central chain. For practical calculations, the following values are used, K_1=0.6949eV, K_2= -1.415×10^3 eV and K_3=9.699×10^5 eV. These values are so chosen that the interchain interaction becomes appreciable only when $|q_\ell - (-1)^\ell q_0| \geq 2 q_0$ and $\ell_0 \geq 10^2$.

Fig.11 demonstrates the adiabatic energy surface of the ground state E_g and that of the first excited state ($\equiv E_{x1}$), thus obtained, as a function of Δq and ℓ_0. While θ is determined to minimize E_{x1}, since we are going to clarify the relaxation path of the excited state. All the energies are referenced from the energy of the ionic true ground states (Δq =0, ℓ_0=0) shown in Fig.7. In Fig.11(a), the region with $\Delta q < 0.5$ is still the I-phase, which has the SDW type order already shown in Fig.8(a).

Nevertheless, if we go up from this ionic true ground state (Δq =0, ℓ_0=0) to the plateau region ($\Delta q \cong 0.5$ and $\ell_0 \geq 40$) of Fig.11(a), the N-domain appears. In Fig.12, we have shown charge- and spin-density distributions of this N-domain by solid lines, taking the case $\Delta q = 0.5$ and $\ell_0 = 50$ as a typical example. From Fig.12, we can see that the original SDW type order inside of the domain have now disappeared, and a CDW type order newly appears instead, although the outside of the domain still remains unchanged. According to this calculation[11], this domain boundary between the I-phase and N-one has both

a charge and a spin.

In this plateau region of Fig.11(a), there are various shallow local minima, one of which is shown in an enlarged inset of the right-hand side. The presence of these local minima is mainly due to the discreteness of the lattice, and makes the N-domain stable and long-lived. As Δq and ℓ_0 increase further ($\Delta q \geq 0.5$, $\ell_0 \geq 50$) from this plateau region, E_g also increases further. This increase is mainly due to H_{inter} given by eq.(12), and partly due to the intrinsic energy difference between the I-phase and the N-one shown in Fig.7.

Fig.11(b) and (c) show front and back views of the adiabatic energy surface of the lowest excited state E_{x1}. At around the origin ($\Delta q = 0, \ell_0 = 0$), or at the Franck-Condon state, a local minimum appears, and it is due to the CT exciton. We will see this Franck-Condon region later in detail. There is another local minimum at around $\Delta q = 0.5$ and $\ell_0 = 45$, and it corresponds to the excited state of the N-domain. In Fig.12, we have also shown its charge- and spin-density distributions by dashed lines. We can see the same CDW and SDW type orders as that of the ground state, except the domain boundary. As Δq and ℓ_0 increase further ($\Delta q \geq 0.5$, $\ell_0 \geq 50$), E_{x1} also increases further. This increase is again mainly due to H_{inter}, and partly due to the intrinsic energy difference between the I-phase and the N-one. Thus, H_{inter} is essential to make the N-domain locally stable.

In Fig.13, we have shown both E_g and E_{x1} as a function of ℓ_0, along the steepest ascending line from the true ionic ground state to the N-domain. This line, denoted by red in Fig.11(a), is determined to be always orthogonal to the equi-potential line. In the adiabatic energy curve of E_{x1}, we can see two local minima mentioned before. The first one at around $\ell_0 = 0$ corresponds to the CT exciton as mentioned before. While the second one at $\ell_0 = 45$ corresponds to the N-domain, which is a little above the CT exciton. Moreover, these two minima are clearly separated by a high adiabatic potential barrier with each other. As shown in Fig.2(c) and Fig.12, we have two boundaries between the I-phase and N-one. The energy increase to create these two boundaries makes a small size N-domain ($\ell_0 < 40$) too unstable in the excited state. It can be stable only when its size exceeds a critical value ($\ell_0 \approx 40$), just like the formation of a gaseous bubble in an overheated liquid. We should also note that it is the characteristic only of the excited state E_{x1}. While, in the ground state energy curve E_g shown in Fig.13, we have not such a high barrier, but only low barriers as shown in the enlarged inset.

Thus, we can conclude that the single CT exciton alone can never result in the macroscopic N-domain formation straightly. Only when our system is excited by a large excess electronic or vibrational (phonon) energies than the single exciton state, it can overcome this high barrier and results in the macroscopic N-domain formation, as shown in Fig.13. In other words, only when we have such a large excess energy at the very beginning of the relaxation, this excess energy can be converted into the exciton proliferation, and can induce other various nonlinear processes during the relaxation.

In this connection, let us focus our attention only on the adiabatic potential energy surface of

Franck-Condon region of Fig.13. It is shown in Fig.14 in detail. We can see that the exact local energy minimum associated with the CT exciton is, not just at the origin ($\ell_0 = 0$), but at around the point with $\ell_0 \approx 7$ and $\Delta q \neq 0$. This is nothing else but the ordinary self-localization of the CT exciton[1]. Since our system has a high intrinsic nonlinearity, however, even this single CT exciton can somewhat proliferate during this self-localization process, and grow up to be a small cluster composed of few CT excitons. Nevertheless, because of the high energy barrier mentioned before, this growth is limited only within the microscopic scale. After this limited lattice relaxation within the Franck-Condon region, the resultant cluster will disappear nonradiatively as schematically shown in Fig.14. This theoretical result is consistent with the recent experiments[9,20]. This small scale proliferation accompanied by the self-localization is already well-known in various other quasi one-dimensional insulators[2].

Finally, it should be noted that the process described above is only the early stage or the nucleation process of the macroscopic photoinduced phase transition. The neutral domain thus created will stay at the aforementioned shallow local energy minimum of E_g for a long time than the one oscillation period of phonon. Hence, during this stay, it can move diffusively within a chain, and can merge with other N-domains created by other photons, and results in a global phase transition.

5.5 High energy optical excited states in SDW state

As mentioned above, the high energy optically excited states are responsible for the photoinduced phase transition, rather than the single CT exciton. Hence, we have to clarify the nature of these highly excited states of the SDW state. In the Franck-Condon state, as mentioned before, quantum and dynamical natures of the electron-phonon interaction does not work, since the lattice is fixed at the ground state configuration. As is well known, this electron-phonon interaction is a retarded one, which can start working quantum-mechanically about 10^{-12} second after the optical excitation. While, the inter-electron Coulomb interaction, being the instantaneous force, will dominate the nature of highly excited states, since the starting ground state is the SDW state. In order to clarify this effect, however, the unrestricted Hartree-Fock approximation is too crude, and we have to take into account effects of quantum fluctuations of itinerant electrons due to the Coulomb interaction. For this reason, we clarify higher optical excited states of the half-filled SDW state, using a more simple one-dimensional extended Hubbard Hamiltonian($\equiv H_{ex}$). It is given as

$$H_{ex} = -T_i \sum_{\ell,\sigma} \left[\left(C^{+}_{\ell,\sigma} C_{\ell+1,\sigma} \right) + (\text{h.c.}) \right] + U \sum_{\ell} n_{\ell,\alpha} n_{\ell,\beta} + V_0 \sum_{\ell} n_{\ell} n_{\ell+1} . \quad (13)$$

When $U > 2V_0$, this Hamiltonian gives the SDW state with the antiferromagnetic order, just like Fig.6(b), although we have neither Δ nor the dimeric electron-phonon interaction. While, when $U < 2V_0$, we have the CDW state just like Fig.6(a). Moreover, when U exceeds $2V_0$ only a little, we get such a situation similar to Fig.7 that this SDW state is just below the CDW one. Thus, as far as the Franck-Condon states are concerned, we can well reproduce the situation realized in the TTF-CA crystal, using this simple model. While the benefit of this simple model is that we can calculate higher excited states, using the non-Grassmann path-integral theory[21], which takes the coulombic inter-electron quantum correlations

straightforwardly. By this theory, various optical spectra have been calculated under the bistable condition[22,23],

$$(U\text{-}2V_0) << U. \quad (14)$$

From these results, we can conclude that high energy optical excited states with energies a few times greater than the CT exciton are the random excitations of several CT excitons coupled with many magnons or spin-excitations. As is well known, in the SDW state, we have the Goldstone mode called magnon, whose energy is gapless and has a linear dispersion. When the SDW state has a small dimerization, a small energy gap opens in this dispersion. However, the above characteristic of high-energy excited states is not affected.

One can think of such a possibility that, a macroscopic CDW domain (N-domain) can be directly excited at once, just after the Franck-Condon transition from the SDW ground state by using only a few photons. However, it is impossible since these two states are "macroscopically orthogonal" with each other. It is theoretically obvious that a dipole operator of a photon can change the state of only one electron, before and after the transition. An electron and a hole thus created by this dipole transition can also change the states of many other surrounding electrons through the Coulomb interaction. However, this is nothing else but random scattering, being far from making a well-defined macroscopic spatial order at once. The macroscopic spatial order can be established only after this highly excited state is cooled down to some local minimum, by dissipating its excess energy one by one into the phonon system, which acts as an heart reservoir, just as shown in Fig.13. This step-wise nature, being not at once, is the essence of the macroscopic order formation, resulting in the PSPT.

5.6 Simulation by classical time-dependent theory

Thus we have seen the path of the photoinduced I-N transition in detail, making use of the calculated adiabatic potential surface. As for the real time dynamics of this transition, however, we still have various problems left unclear. In this connection, very recently, Yonemitsu[24] has undertaken a simulation study for the real time dynamics of this transition, using a classical and time-dependent theory. In this simulation, Yonemitsu has newly introduced the following two points. 1) In eq.(2), T_i is assumed to depend on real time ($\equiv t$), so that it can describe, not only the original transfer energy, but also the charge transfer type electron excitation, coming from the vector potential($\equiv A(t)$) of an externally applied classical photon field. This $A(t)$ is assumed to be a sinusoidal function of t with an energy ($\equiv \omega_{ext}$), which is almost same as that of the CT exciton. 2) In eq.(5), the kinetic energy term $(\partial q_\ell / \partial t)^2 / 2$ is also added to describe the classical motion of the lattice.

At t=0, the whole system is assumed to be in the electronic ground state of the I-phase, with a small but finite velocity $\partial q_\ell / \partial t$ and lattice distortion $(q_\ell - (-1)^\ell q_0)$, coming from the thermal fluctuation. From this initial condition, the time evolution of the whole system is calculated iteratively within the classical, adiabatic and Hartree-Fock approximations. As one of its results, the total induced charge ρ_I at the CA site is shown in Fig.15 as function of t, wherein N_{ext} specifies the exciting time period, $0 < t < N_{ext}\, 2\pi / \omega_{ext}$, during which the external photon filed is switched on and turned off afterwards. We can see that only when

N_{ext} exceeds its threshold value $N_{ext} \geq 4$, ρ_I can decrease down from 1 to about 0.35. That is, the photoinduced I-N transition can be attained only under this threshold condition.

6. Quantum nonlinear nonequilibrium dynamics and initial condition sensitivity

In the previous sections, we have been concerned with the classical and adiabatic natures of the TTF-CA, and so, let us now proceed to the early time quantum nonlinear nonequilibrium dynamics of the PSPT. To theoretically describe this quantum dynamics, however, the practical situation realized by eq. (1) is too much complicated. Hence, we have to simplify our problem, extracting only its essences from the view point of the PSPT. These essential points are summarized into the following five ones.

1. When the exciting photon is resonated to the CT exciton (~ 0.6eV), these excitons are created homogeneously in the 1-d crystal, and hence, the mean inter-exciton distance becomes rather long as compared with the lattice constant. While, just after the intra-molecular excitation (~ 2.2eV), an electron-hole pair is created in a same molecule, with the energy few times greater than the CT exciton. This high-energy pair is electronically unstable even at the Franck-Condon state, and will immediately decompose into several CT excitons, through the inter-molecular Auger decays or other coulombic many-body scatterings. These several CT excitons are expected to be very close to each other around the original molecule. Therefore, the difference in the initial condition between the CT excitation and the intra-molecular one is reduced only to the difference of the initial distance between the adjacent photogenerated CT excitons. We also have many other excitations in between(0.6eV~ 2eV), and corresponding spatial arrangements of the CT excitons will be different each other, even if the total absorbed photonic energies are same. To describe this difference, we have schematically shown in Fig.16, typical three cases of such spatial arrangements, that is, sparse (Fig.16(a)), close (Fig.16(b)) and moderately distant (Fig.16(c)) excitations. Using these three typical arrangements of excitons, we will clarify the initial condition sensitivity.

2. There must be a hidden but intrinsic multi-stability. A false ground state has to be just above the true one, and the energy difference between them per unit volume should be larger than the thermal energy, but should be much smaller than the visible photon energy as schematically shown in Fig.1, Fig.7, Fig.13, and Fig.17.

3. There must be a nonlinear mechanism, through which the excitons can proliferate. This mechanism should be efficient enough to overcome various radiative and nonradiative decay channels of the CT excitons. These decay channels will act in every intermediate stages of the relaxation, to hinder the proliferation as schematically shown in Fig.17.

4. At the final state of the Franck-Condon transition, a large excess energy should be given to the excitons, as schematically shown in Fig.13 and Fig.17. By using these excess energies, the initially created excitons can proliferate, under the energy conservation law.

5. The resultant domain should be a local minimum in the adiabatic potential surface of the ground state, so that this domain can have a sufficiently long lifetime and is worth to be called the PSPT. Thus, the initially created excitons have to go through various intersections of the potential surfaces diabatically, so that it can finally reach to the local energy minimum, not in the excited state potential surface, but in the ground state one, as shown schematically in Fig.13 and Fig.17. In this sense, the adiabatic approximation is not enough to describe the real time dynamics of the PSPT.

6.1 Model Hamiltonian for quantum dynamics

In order to describe the above points from a unified theoretical point of view, Mizouchi et al have used a more simplified model than eq. (1), and have clarified the early time quantum dynamics of the PSPT. They have studied the following many-exciton system coupling strongly with Einstein phonons in a quasi one-dimensional crystal[25,26]. Its Hamiltonian $(\equiv H_{me})$ is given as,

$$H_{me} = E_e \sum_{\ell} B_{\ell}^{\dagger} B_{\ell} - T_e \sum_{\langle \ell, \ell' \rangle} [B_{\ell}^{\dagger} B_{\ell'} + (\text{h.c.})] + \omega \sum_{\ell} b_{\ell}^{\dagger} b_{\ell} - \omega S^{1/2} \sum_{\ell} B_{\ell}^{\dagger} B_{\ell} (b_{\ell}^{\dagger} + b_{\ell})$$

$$- \sum_{\ell, \ell'(\neq \ell)} V_e(|\ell - \ell'|) B_{\ell}^{\dagger} B_{\ell} B_{\ell'}^{\dagger} B_{\ell'} + \sum_{\ell, \ell'(\neq \ell)} G(|\ell - \ell'|) B_{\ell}^{\dagger} B_{\ell} (B_{\ell'}^{\dagger} + B_{\ell'}) + H_{ic}, \qquad (15)$$

where $B_{\ell}^{\dagger}$ is a creation operator of an exciton (a quasi boson) at a site ℓ with an energy E_e, and T_e is the transfer energy between ℓ to its neighboring site ℓ', and the bracket $\langle \ell, \ell' \rangle$ denotes this neighboring relation. $b_{\ell}^{\dagger}$ is the creation operator of the Einstein phonon at site ℓ with a frequency ω, and S is the exciton-phonon coupling constant. $V_e(\ell - \ell')$ denotes a phenomenological attraction (or interaction) between two excitons at sites, ℓ and ℓ'. In the present theory, we will not specify its microscopic origin in detail. It can be an effective attraction due to the van der Waals force, other coulombic interactions, or some inter-site exciton-phonon couplings. The occupancy of a single site by more than one exciton is excluded from the beginning. $G(\ell - \ell')$ in the sixth term represents the third-order anharmonic inter-exciton coupling. Through this anharmonicity, an exciton at site ℓ' is created or annihilated by another exciton at site ℓ. Such a nonlinearity results from the long range Coulomb interaction between electrons and holes constituting excitons. The Coulomb interaction itself is originally quartic with respect to these Fermion operators, being quite nonlinear from the beginning. Hence, to take into account this nonlinearity or anharmonicity is quite natural. However, through this nonlinearity the excitons can proliferate, as shown later in detail. Furthermore, since this coulombic nonlinearity is an instantaneous force with no retardation effect, it can cause the proliferation readily.

The last term H_{ic} of eq.(15) denotes the interchain interaction.

$$H_{ic} = \sum_{N} h(N) \sum_{i} |N,i><N,i|, \qquad N \equiv \sum_{\ell} B_{\ell}^{\dagger} B_{\ell}, \qquad (16)$$

where N denotes the total number of excitons, and i specifies each quantum state ($\equiv |N, i>$) within the N exciton states. Thus, $\sum_i |N,i><N,i|$ is a projection operator into the N exciton state. While h(N) denotes an effective potential given from the other chains to this N-exciton system, when it is created in the central chain on which we focus. This potential h(N) is assumed to depend only on the total number N, irrespective of various spatial arrangements of N excitons. This functional form is also assumed to be quite nonlinear in the sense that it is almost zero when N is smaller than its critical value $N_c(\sim 10)$, while it becomes nonlinearly appreciable when N exceeds N_c. For such h(N), we have taken the following form as

$$h(N)=\omega\sum_{j=0}^{4}a_j N^j,\quad a_4=3.27\times10^{-4},\quad a_3=-7.08\times10^{-3},\quad a_2=4.98\times10^{-2},$$

$$a_1=2.03\times10^{-2},\quad a_0=-6.33\times10^{-2}. \qquad (17)$$

The role of this interaction is almost same as that of eq.(12), and it makes the domain with N_c excitons locally stable, as schematically shown in Fig.17.

It should be noted that the present exciton-phonon system is our relevant system, and is also assumed to couple linearly with the photon field and acoustic phonon modes, which act as a heat reservoir during the relaxation, although they are not written here explicitly.

6.2 Relaxation and occurrence or nonoccurrence of the PSPT

Using Fig.17, let us now schematically explain the characteristics of the relaxation processes, which lead to the occurrence or nonoccurrence of the PSPT. The solid curve and thin dotted curves denote adiabatic potential surfaces of the ground and excited states. The global minimum of the lowest curve denotes the ground state. The other local minima 1, 2, ... of this curve denote the lowest energy states with 1, 2, ... excitons, respectively. The local minimum N_c has the lowest energy among these local minima 1, 2, ... The upward solid arrows denote the initial photoexcitations. The dashed-and-dotted arrows denote the main relaxation paths. The downward dotted arrow denotes radiative decay of excitons. These nonradiative and radiative decays are brought about through the interaction between our relevant system and the acoustic phonon and photon fields mentioned before. We also have assumed a multi-stable situation where the lowest energy of (N+1)-exciton states is energetically close to that of N-exciton state. This condition is realized when (E_e-S) and $V_e(1)$ are well balanced in eq.(15) as, $(E_e-S)\approx V_e(1)$.

In Fig.17, the excitons are created from the ground state by photoabsorption (the leftmost upward solid arrows). In the next, the exciton relaxes along the following two paths. One path is the vibrational (or lattice) relaxation, where the system changes along an adiabatic potential curve of the excited state (the dashed-and-dotted curves in Fig.17). The photoexcited state along this path has a large excess electronic and vibronic (phonon) energies. The other path is the direct radiative decay (the downward thick dotted arrow in Fig.17). Here, the former path is main one because vibrational relaxation is faster than radiative decay. As seen from this figure, many adiabatic potential surfaces come close to each other at many points. Around such points, the diabatic transition occurs. If the relaxation proceeds toward the right through such processes, the proliferation becomes successful.

As mentioned in section 4, various relaxations can start from almost the same Franck-Condon states, as far as the initially absorbed total photonic energies are same. However, these starts are a little different with each other, according to the way or type of the photoexcitation, because their electronic structures are mutually different. Then, during the relaxation, the difference between these adjacent starts diverges. Some of them quickly return to the ground state nonradiatively, while others proceed toward the right in Fig.17 and stays in multi-exciton states for a long time. Furthermore, among the latter cases, some of them can reach quickly to the destined lowest energy state with N_c excitons. While others, because of the tunneling, reach rather slowly the destined N_c-exciton state, although they relax down quickly only as far as to the lowest potential curve. This is nothing else but the initial condition sensitivity[10].

6.3 Lifetime prolongation

Here we should note about the prolongation of the life time of these various transient states, which appear during the relaxation. As mentioned above, the PSPT is a transient phenomenon, and the system surely goes back to the ground state finally. However, the state generated by the PSPT can become sufficiently stable, and it takes quite a long time to go back to the ground state. This is because the overlap integral between the multi-exciton state and the ground state with no exciton, become smaller and smaller, as the proliferation proceeds from left to right in Fig.17. Hence the transition between them becomes very difficult, even if the photon and the acoustic phonon spontaneously try to induce it through their quantum fluctuations. Thus, the more the decay time elongates, the more the resultant domain becomes large and stable, just as the hen-and-egg relation.

6.4 Iterative method for exciton proliferation

In order to investigate the time evolution of the aforementioned exciton-phonon system, we are now in the stage to derive the master equation under the Markov approximation for the photon field and the reservoir. However, there is a serious numerical difficulty in the direct calculation of this time evolution in the large size systems, because the quantum mechanical treatment of Einstain phonons leads to too large dimensional calculations. Therefore, in order to overcome this numerical difficulty, we derive an iterative equation for the exciton proliferation. The basic idea is schematically shown in Fig.18.

We focus only on the most front of the expanding photoinduced domain, and the contributions from the other excitons, not in this front, are approximated by a mean field. As proliferation proceeds, the position of this front also moves. At the step 1 in Fig.18, the front of the domain is assumed to be in the inside of the box. This box is our relevant system, within which we calculate excitons, Einstain phonons and their interactions, full-quantum-mechanically. We take the size of the box as 4 lattice sites around the front. Inside of this box, we prepare an exciton with an excess energy, and it is represented by a double circle. In the following, we call it "mother exciton". We also prepare several excitons outside of our relevant system (the box), and they are represented by black circles. They are localized at each lattice site, and their energies are fixed to the lowest vibronic ones. We call them "frozen excitons".

Under the existence of these frozen excitons, the Hamiltonian H_{me} of our exciton-phonon system is approximated by H'_{me}, which is defined only within the Hilbert space of the front region as,

$$H'_{me} \equiv E_e \sum_{\ell} B_\ell^\dagger B_\ell - T_e \sum_{\langle \ell,\ell' \rangle} [B_\ell^\dagger B_{\ell'} + (\text{h.c.})] + \omega \sum_{\ell} b_\ell^\dagger b_\ell - \omega S^{1/2} \sum_{\ell} B_\ell^\dagger B_\ell (b_\ell^\dagger + b_\ell)$$

$$- V_e(1) \sum_{\langle \ell,\ell' \rangle} B_\ell^\dagger B_\ell B_{\ell'}^\dagger B_{\ell'} + \sum_{\ell,\ell'(\neq \ell)} G(|\ell - \ell'|) B_\ell^\dagger B_\ell (B_{\ell'}^\dagger + B_{\ell'}) + \sum_{\ell_f} N_{\ell_f} [E_e - \omega S] - V_e(1) \sum_{\langle \ell_f,\ell'_f \rangle} N_{\ell_f} N_{\ell'_f}$$

$$- V_e(1) \sum_{\langle \ell_f,\ell \rangle} N_{\ell_f} B_\ell^\dagger B_\ell + \sum_{\ell_f,\ell} G(|\ell_f - \ell|) N_{\ell_f} (B_\ell^\dagger + B_\ell) + \sum_{N} \hbar(N + N_f) \sum_{i} |N, i\rangle\rangle \langle\langle N, i|, \tag{18}$$

$$N \equiv \sum_{\ell} B_\ell^\dagger B_\ell, \quad N_f \equiv \sum_{\ell_f} N_{\ell_f}. \tag{19}$$

Here, ℓ and ℓ' now denote the sites only within the front(box). N_{ℓ_f} denotes the average density of the

frozen exciton at a site ℓ_f outside of the front, and hence, this N_{ℓ_f} is a *c*-number. N now denotes the total number of excitons only within the front, and $|N,i\rangle\rangle$ denotes i th eigenstate with N excitons in this front. The first six terms of eq.(18) denote the Hamiltonian within the front. While, the seventh and eighth terms denote the energy of frozen excitons outside of the front. The ninth and tenth terms denote the interactions between the front and its outside. The last term is the interchain interaction, in which the presence of the frozen exciton is already taken into account.

Using this eq.(18) and the master equation method, we can now describe the dynamics of the exciton proliferation in this front. As seen in the sixth term of eq.(18), the mother exciton can proliferate through the original $G(\ell-\ell')$ by using her excess energy, and can make her "daughter exciton"(step 2 in Fig.18). However, we can see that even the frozen excitons can also help this proliferation as an external mean field, through the tenth term of eq.(18).

Thus, as time goes by, the daughter exciton grows up, and the total number of excitons increases (step 3 in Fig.18). When the total number of excitons in the front increases by 1 from the initial one, we regard the daughter has grown up to be an adult, and approximate that the following generation crossover occurs (step 4 in Fig.18). The mother exciton is replaced by a frozen one, and the daughter exciton is taken as a new mother. Here, as seen from eq.(18), it should be noted that excitons except frozen ones can move between lattice sites in the box. Thus, the exciton density has a non-integer value at each lattice site. Therefore, in the aforementioned crossover, we regard the excitons whose densities are the largest and the second largest in the box, as the mother exciton and the daughter one, respectively.

Furthermore, we assume the new mother inherits the excess energy, after this generation crossover. We determine this excess energy of the new mother so that the total energy in the system is conserved before and after this generation crossover. However, this excess energy becomes smaller and smaller than the starting one, because of the dissipation or relaxation.

By this crossover, the front moves, and accordingly the box moves. In fact, in the case of Fig. 18, the front moves one lattice site towards the right. Then, we focus again only on this new front, and iterate the aforementioned procedure, until the excess energy is exhausted through the interaction between our relevant system and the aforementioned heat reservoir. During this iteration, the size of the box around the front is kept unchanged as shown Fig.18. Therefore, without enlarging our computer memory, we can numerically calculate the time evolution dynamics of a large number of excitons in the large system.

Hereafter, we call one iteration (from the step 1 to the step 3 in Fig.18) "one generation". We should also note that this iterative procedure is justified, when T_e is small as compared with $S\omega$ in eq.(15).

6.5 Numerical results

Let us now specify the values of the parameters in eq. (15). Our purpose here is not a comprehensive study for eq.(15), but to study one of typical situations realized by a set of parameters values, which is in compliance with the aforementioned five points, and makes the PSPT quite successful. As one of such examples, the following values are taken; $\omega = 0.1\text{eV}(\hbar = 1)$, $E_e/\omega = 9.5$, $T_e/\omega = 1.0$, S=8, $V_e(1)/\omega = 1.7$, $G(1)/\omega = 0.2$, $G(2)/\omega = 0.1$, $G(3)/\omega = 0.067$, $G(4)/\omega = 0.05$, $G(5)/\omega = 0.04$ and zero for other G's. N_c is taken to be 10. The radiative damping rate of the exciton is assumed to be 10^{-9} second at the Franck-Condon state, and afterward decreases in proportion to the third power of the transition energy, while the damping of the Einstein phonon due to its coupling with the acoustic phonon reservoir is assumed to be

20% of the phonon energy ω. The large S corresponds to the large excess energy at the Franck-Condon state, while finite ω / T_e makes aforementioned diabatic transitions possible.

Here, we start from the initial condition that there are two localized excitons, just as shown in Fig.16. One of them is an exciton created by the Franck-Condon excitation from the ground state. This is a mother exciton. While, the other exciton is taken as a frozen one, for the reason mentioned before. In the following, the distance between these two excitons at the initial state is represented by d_0. Results are shown in Fig.19, and the time evolution dynamics become different according to this d_0. The net exciton proliferation occurs only when d_0=2, 3 and 4. When d_0=1 and ∞, the number of excitons increases a little from 2 only at early time, however, the net proliferation does not occur finally. Therefore, the initial distance between excitons should be moderate in order to get net proliferation. In the too far distant case ($d_0=\infty$), the nonlinearity among excitons does not work, and it leads to no net proliferation. On the other hand, in the too close excitation case (d_0=1), too strong nonlinearity works, and it leads to the exciton annihilation rather than its proliferation. Therefore, the critical nonlinearity is necessary to realize net proliferation. Here, the case with $d_0=\infty$ corresponds to the CT excitation below the threshold mentioned in section 4. In the intra-molecular excitation case, d_0 takes various values within the force range of the aforementioned intermolecular Auger decay. Among them, only the successful cases can finally survive (d_0=2, 3 and 4). Furthermore, even when the net proliferation occurs, the time evolution behavior of each proliferation is not same but chaotic, according to the value of d_0. For example, when d_0=4, the proliferation occurs more slowly than the other proliferating cases (d_0=2 and 3). These results show the initial condition sensitivity still exists even when the proliferation is successful.

In Fig.20, we show a spatial arrangement of excitons at the beginning of each generation (the step 1 in Fig.18), taking the case with d_0 = 3. Here, G_e denotes the generation, and the time ($\equiv$ t) is measured from the beginning of the first generation. The black circle and the double one denote a frozen exciton and a mother one, respectively. Especially, the white circle with a black one denotes the mother exciton created by the Franck-Condon excitation from the ground state. The values under each arrangement denote the exciton densities in the front, just before the generation crossover (the step 3 in Fig.18). The values of frozen exciton densities are almost equal to 1, and hence they are not written explicitly.

From Fig.20, we can see that the two mutually unconnected clusters of excitons are formed during the first four generations (G_e=1 to 4). At G_e =5, however, these two clusters have merged with each other, and this merged one grows longer and longer, until the total number of excitons reaches N_c. Thus, we can see the dynamics of the exciton proliferation is not monotonic but fluctuating, since our system is quantum-mechanical.

6.6 Pattern formation dynamics in two-dimensional cases

Let us now proceed from the 1-d case to two-dimensional ones. In this case, we face to a new problem absent in the 1-d systems, that is, the pattern formation dynamics of the exciton domain. Very recently, Yabuki[27] has undertaken a theoretical study that extends the previous theory of Mizouchi [26] for 2-d cases, so that, it can describe this pattern formation dynamics, keeping other aspects of this theory except the dimensionality almost same. He has concluded that occurrence or nonoccurrence of the PSPT is closely related to spatial anisotropy or isotropy of the interexciton interaction $V_e(|\ell - \ell'|)$ in eq.(15).

According to the standard theory of exciton by Knox[28], $V_e(|\ell - \ell'|)$ can be estimated by the Wannier functions of the electron and the hole constituting the exciton. If these functions are well localized around their central lattice site, we get a well isotropic $V_e(|\ell - \ell'|)$, just like the van der Waals force. This situation is realized in the rare gas solids. While, in the cases of itinerant electron systems, the Wannier functions of electron and hole are usually extended from its central lattice (or atomic) site to its several neighboring ones, widely and oscillatory. Moreover, the symmetries of these Wannier functions can often be anisotropic, like p- and d-orbitals. Thus, in some case, $V_e(|\ell - \ell'|)$ can become repulsive between the second nearest neighboring sites, although it is mostly attractive between the first neighboring ones. This anisotropic situation,

$$V_e(1) > 0, \quad V_e(\sqrt{2}) < 0, \quad |V_e(1)| > |V_e(\sqrt{2})|,$$

is schematically shown in Fig.21, wherein, a 2-d square lattice is used. Such an anisotropy is shown to make the resultant exciton domain pattern "fractal", just like the fjord of Norway coast[27], and it finally leads to a quite successful PSPT.

One of results of this theoretical calculation is shown in Fig.22 and Fig.23, wherein a typical inisotropic parameters are used, $V_e(1)/\omega = 1.152$, $V_e(\sqrt{2})/\omega = -0.528$. As seen in these figures(Fig.22, 23), at the beginning, successive 8 light pulses with an equal time interval ($1000 \times (2\pi\omega^{-1})$) are shone on to a 12×12 square lattice. The excited lattice sites by these 8 light pulses are quite random within this 2-d lattice. During this pulse excitation, the total energy ($\equiv E_{ten}$) and the total exciton number ($\equiv N_{exc}$), of course, rapidly increase. After this excitation, E_{ten} decreases but N_{exc} increases rather slowly, because of the dissipation and tunneling effects mentioned before in detail in connection with Fig.17 and Fig.19. In order to see the transient time evolution of the domain pattern, typical four time points (a), (b), (c) and (d) are chosen from Fig.22, and corresponding patterns are shown in Fig.23.

The time point (a) is just after the pulse excitation is turned off, while (d) is long after this excitation, and (b) and (c) are in between. In Fig.23, the gray circle denotes the newly generated exciton, while the black circle denotes the frozen exciton, which is already generated until the previous time point. In Fig.23 (a), we can see many peninsula structures stretched outside of the domain with bays and gulfs between them. This fractal or fjord structure, which appears just after the pulse excitation, is due to the aforementioned anisotropy. These bays and gulfs, thus generated, are afterwards filled up one by one very slowly through the quantum tunneling, as seen in Fig.23(b) and (c), and finally, we get a large size domain with a simple structure, as shown in Fig.23(d). This filling-up effect mainly comes from the tenth term of eq.(18), that is, the frozen excitons in the coast line of these bays and gulfs, make the proliferation quite probable. This filling-up effect is also highly nonlinear and cooperative as seen from the time dependencies

of E_T and N_{exc} shown in Fig.22.

Various isotropic cases are also studied in the same way, and compared with the anisotropic cases[27]. However, in these isotropic cases, we can have only small size domains with simple structures. Thus, the anisotropy is shown to play a very important role in the transient pattern formation and the final PSPT.

7. Difference between photoinduced nonequilibrium phase and high temperature equilibrium phase

According to these progresses of experimental and theoretical studies on photoinduced phase transitions, a new but quite basic question has now emerged. That is, how the photoinduced phase is practically different from the high temperature equilibrium one. As mentioned occasionally, the photoinduced phase is a nonequilibriun phase, brought about through the multi-stability, or the pseudo-degeneracy of the ground state. However, when this multi-stable situation is realized in our system, a state, similar to the false ground state, is also inferred to appear as an equilibrium phase at high temperatures, that is, through the ordinary thermal phase transition.

In fact, both this photoinduced phase at low temperature and the equilibrium one at high temperature are observed as shown in sections 3 and 5, and these two phases are quite similar with each other. Thus the aforementioned issue becomes quite serious and significant.

7.1 Photoinduced phase transition in organo-metallic complex crystal

However, recent experiments on the photoinduced phenomenon in the organo-metallic complex crystal $[Fe(2\text{-}pic)_3]Cl_2 \cdot EtOH$ (, 2-pic = 2-amino-methyl-pyridine,), have opened a new prospect in the study for the aforementioned difference. In this crystal, as shown in Fig.24, an Fe^{2+} ion and its neighboring six nitrogen atoms of three 2-pic molecules, are making a complex, which approximately has an O_h symmetry. As schematically shown by dashed lines of this figure, this metal complex is bonded with other three neighboring ones through the hydrogens, and these hydrogen bonds result in inter-complex interactions. An Fe^{2+} ion has six electrons in its 3d orbitals (t_{2g}, e_g), and these electrons are in a crystal field, whose symmetry is almost O_h as mentioned before. At absolute zero temperature, these 6 electrons, being in the three t_{2g} orbitals, become diamagnetic (S=0) as shown in Fig.24. This diamagnetic phase has a strong light absorption band at around 2eV, and the color of this crystal is deep red. While, at about 120K, a first order phase transition occurs from this diamagnetic phase to a paramagnetic one (S=2), as shown in Fig.20, and the color of the crystal changes from deep red to yellow.

On the other hand, Ogawa et al[30] have recently discovered the photoinduced phase transition in this crystal. Shining 1.8eV light on to the low temperature diamagnetic phase of this crystal, they have succeeded to generate a macroscopic paramagnetic domain. By this photoinduced phase transition, as shown in Fig.25, the color of the crystal changes from deep red to yellow, which is quite similar to the yellow of the high temperature paramagnetic phase. They also have found the bi-directional nature of this photoinduced diamagnetic $\leftrightarrow$ paramagnetic transition, and the threshold type behavior just like the case of TTF-CA mentioned in section 4.

In connection with this discovery, very recently, Tayagaki el al[31] have also succeeded in observing Raman scattering spectra of these three phases, the low temperature diamagnetic phase, the high temperature

paramagnetic phase, and the photoinduced paramagnetic phase at low temperature. The resultant three Raman spectra are shown in Fig.26. We can clearly see that the photoinduced phase is different from the other two phases, especially in the shaded region, although other spectral regions are similar to that of the high temperature paramagnetic phase. It should be noted that this difference between the three phases is a macroscopic difference, being not an ordinary photoinduced structural change which, very often occurs only in a microscopic region of optically excited crystals. Tayagaki el al have assigned this difference in the shaded region to come from a new parity violation of the aforementioned O_h symmetry around the 3d orbital[31].

According to the present status of our experimental study on this organo-metallic complex crystal, however, a new interaction which originates this new parity violation can not be clarified sufficiently, because this crystal is really complex, as we can easily infer from Fig.24.

7.2 Broken symmetry only in photoinduced nonequilibrium phase

It is quite clear that this new broken symmetry (or new parity violation) does not occur in both two equilibrium phases (the low temperature diamagnetic phase and the high temperature paramagnetic one), but occurs only in the photoinduced nonequilibrium phase at low temperature. This difference between the equilibrium phase and the nonequilibrium one, if once well-established conceptionally, will greatly affect on our studies for photoinduced phase transitions in various other materials. Because, it means that, we can discover a new interaction and its resultant broken symmetry through the photoinduced nonequilibrium phase at low temperatures, even if this new interaction is not clearly observed in any equilibrium phases, such as the true ground state or high temperature equilibrium phases.

Here, we should note our conventional way to recognize a new interaction to exist and operating in a material. According to our ordinary way of recognition, such an interaction (,or its resultant broken symmetry,) is often neglected or regarded not to exist at all from the beginning, if it is not clearly observed in any equilibrium phases. Aforementioned experimental result[31], however, clearly tells us that it is a prejudice, which we have to overcome.

7.3 Two-dimensional extended Peierls-Hubbard model

In order to make this point clear, Haui et al[3,32] theoretically studied a model system which is more simple and standard than the organo-metallic case. Its purpose is to theoretically describe the situation that a new interaction ($\equiv H_n$) appears explicitly only in the low temperature nonequilibrium phase as a broken symmetry, under the condition that it is almost completely hidden in any other equilibrium phases at low and high temperatures. To address such an issue theoretically, they introduced a square lattice composed of N_t sites and N_t electrons, which are strongly coupling with site-localized phonons. Then this two- dimensional (2-D) many-electron system has the following Hamiltonian ($\equiv H_{PS}$) , which we often call Peierls-Hubbard model,

$$H_{PS} = -T_D \sum_{<\ell,\ell'>,\sigma} C^{+}_{\ell,\sigma} C_{\ell',\sigma} - S_D \sum_{\ell} Q_\ell (n_\ell - 1) + \sum_{\ell} V_{ah}(Q_\ell) - \frac{1}{2M} \sum_{\ell} \frac{\partial^2}{\partial Q_\ell^2} + H_n \ , \qquad (20)$$

$$H_n = U_D \sum_{\ell} n_{\ell,\alpha} n_{\ell,\beta} \ , \qquad (21)$$

where T_D denotes the transfer energy of an electron between two neighboring lattice sites, and ℓ is a 2-D vector with the Cartesian components ℓ_x and ℓ_y. S_D denotes the coupling constant between electrons and the site-localized phonon mode whose dimensionless coordinate is Q_ℓ. $V_{ah}(Q_\ell)$ denotes a potential energy of this site-localized phonon mode, while M is the effective mass of this mode, and its dimension is $(\text{energy})^{-1}$. This potential $V_{ah}(Q_\ell)$ is assumed to be highly anharmomic as

$$V_{ah}(Q_\ell) = (aQ_\ell^2 - bQ_\ell^4 + cQ_\ell^6), \tag{22}$$

where a, b, c are 2i-th (i =1,2,3) expanding coefficients of $V_{ah}(Q_\ell)$ with respect to Q_ℓ. Such an anhamonicity is necessary to make various thermally induced and photoinduced phases stable, and also to make phase transitions first order ones. The last term H_n is the aforementioned new interaction on which we focus. In the present case, for simplicity, we assume that this H_n is a weak on-site Coulomb interaction as shown eq.(21). It is expected to bring an SDW type broken symmetry, and competes with a CDW type order which surely comes from the strong electron-phonon coupling S_D in this 2-D half-filled many-electron system.

7.4 Mean field theory and phase diagram

Within the mean-field theory and the adiabatic approximation ($M \to \infty$), H_{PS} is approximated by a Hartree-Fock Hamiltonian ($\equiv H_{HF}$) which is given as

$$H_{HF} = -T_D \sum_{<\ell,\ell'>,\sigma} C^+_{\ell,\sigma} C_{\ell',\sigma} - S_D \sum_\ell Q_\ell (n_\ell - 1) + \sum_\ell V_{ah}(Q_\ell) + U_D \sum_{\ell,\sigma} \left(\langle n_{\ell,-\sigma} \rangle n_{\ell,\sigma} - \langle n_{\ell,-\sigma} \rangle \langle n_{\ell,\sigma} \rangle / 2 \right), \tag{23}$$

wherein $\langle n_{\ell,\sigma} \rangle$ denotes the thermal average of $n_{\ell,\sigma}$, and it should be determined self-consistently. As for Q_ℓ, we assume that the lattice distortion has a staggered order in both two directions of the square lattice as,

$$Q_\ell = (-1)^{\ell_x + \ell_y} Q_0 \ . \tag{24}$$

Here Q_0 is the amplitude of the CDW or the Peierls type distortion. Correspondingly, $\langle n_{\ell,\sigma} \rangle$ is also assumed as

$$< n_{\ell,\sigma} > = \tfrac{1}{2} + (-1)^{\ell_x + \ell_y} \delta n_\sigma \ , \tag{25}$$

where δn_σ again denotes the amplitude of the density wave of electrons with $\sigma(=\alpha, \beta)$ spin, and this wave also has the double period for both two directions of the square lattice. When the strong coupling and the weak correlation condition ($S_D > T_D \geq U_D$) is satisfied, the ground state of this system is expected to be a CDW type insulator, in which two electrons with up and down spins make a strongly bound singlet pair, and this pair occupies a single site every two sites, along both the x and y axes of this 2-D lattice. While, its high temperature phase will be the ordinary paramagnetic metallic state, although it has a very weak CDW type order, since this model has the complete nesting.

As one of the typical examples to describe this situation, we take the following parameter values, $T_D = 0.3\text{eV}$, $S_D = 1.0\text{eV}$, $U_D = 0.3\text{eV}$, $a = 4.445\text{eV}$, $b = 2.642\times10^3\text{eV}$, $c = 5.487\times10^3\text{eV}$. In the present study, periodic boundary condition is imposed on a 16□16 square lattice whose total number of sites is $N_t = 256$. Figure 27 shows the phase diagram obtained by this mean field theory, and Q_0 is plotted as a function of temperature. The abrupt change of Q_0 at a critical temperature 305K (□T_C) indicates that below T_C the whole system is in the CDW type insulating state in which up- and down-spin electrons make a strongly bound singlet pair ($\delta n_\alpha = \delta n_\beta > 0$, $Q_0 \neq 0$). While, above T_C this system changes into a paramagnetic metallic state ($\delta n_\alpha = \delta n_\beta = 0$, $Q_0 = 0$). This phase transition is the first order, and it just comes from the anharmonicity of V_{ah}, in contrast the case of harmonic phonons, which result in the ordinary second order CDW-metal transition. Thus, the anharmonicity is necessary to separate various equilibrium and nonequilibrium phases by high adiabatic energy barriers, and to make them locally stable.

Figure 28(a) shows us the free energy (per site) at zero temperature in the two-dimensional space spanned by the lattice distortion amplitude Q_0 and the SDW type order parameter ($\delta n_\alpha - \delta n_\beta$). There are two types of minima: the global one at finite lattice distortion $Q_0 = 0.154$ and a shallow one without lattice distortion. They are both locally stable and separated by a barrier of 0.01eV.

As already mentioned in the last section, the electron-phonon coupling results in the Peierls distortion $Q_0 \neq 0$ and the CDW type electronic order ($\delta n_\alpha = \delta n_\beta > 0$), while the on-site Coulomb interaction yields the SDW type electronic order ($\delta n_\alpha = -\delta n_\beta > 0$). Based on the present set of parameters, the CDW order apparently overwhelms the SDW one in the ground state, due to the very strong electron-phonon coupling ($S_D > U_D$). However, this SDW order will also be able to appear as a locally stable false ground state or a nonequilibrium phase, as far as U_D is finite. From Fig.28(a), we can see that, the global minimum, being the true ground state, has a finite lattice distortion with no SDW order. However, we can also see that there is another local minimum, being a false ground state, which has a finite SDW order without lattice distortion. Therefore it is quite clear that the SDW order appears in the false ground state, although it is hidden in the true ground state.

Let us now turn to the cases of finite temperatures. Figures 28(b), (c) and (d) show us the free energy (per site) at a sequence of temperatures 170K, 200K and 400K, respectively. The SDW order remains as a locally stable nonequilibrium state at T=170K, as shown in Fig.28(b), although this order has significantly

decreased from that of the zero temperature. While, at much higher temperature T=200K shown in Fig.28(c), we can see the two free energy minima corresponding to the metallic state ($Q_0 = 0$) and the CDW one ($Q_0 \approx 0.15$), and both of them have no SDW order. It also should be noted that the difference of the free energy between these two states is decreasing due to the increase of temperature. Then, as shown in Fig.24(d), the free energy minimum at $Q_0 = 0$ becomes lower than that of $Q_0 = 0.154$, so that the global free energy minimum now locates at $Q_0 = 0$. That is, the first order thermal phase transition occurs from the CDW state to the metallic one just as shown in Fig.27.

Thus, we have seen that the SDW order is always hidden, although our original Hamiltonian shown in eq.(21) surely has a finite U_D. At zero temperature, the SDW order is completely killed in the true CDW ground state, because, in this state, the electron-phonon coupling makes up- and down-spin electrons to form a strongly bound singlet pair within a single lattice site. While, the high temperature phase is a paramagnetic metallic one, but this high temperature itself also destroys the SDW order. Therefore the Coulomb interaction and its resultant SDW order are almost completely hidden in all the thermal equilibrium phases.

In the present study, the lattice is always assumed to have a staggered order in all possible CDW type phases, and lattice fluctuations are excluded from the beginning. Hence, we may expect that thermal fluctuations below T_C will bring some sign of the SDW order. In this connection, Huai et al also have calculated the SDW order ($\delta n_\alpha - \delta n_\beta$) of the false ground state at each temperature, and found that this order decreases rapidly when temperature is above 100K, and goes to zero at about 183K, which is well blow T_C. Thus even if the thermal lattice fluctuations are taken into account, we will get only a blurred sign of the SDW order.

7.5 Photoinduced phase

Since this SDW order exists only in the false ground state at very low temperature, it may be detected by using photo-excitation. If this system is shone by a strong laser light at low enough temperature, a CT excitation occurs. This excitation is such one that, the up- and down-spin electrons, making a singlet pair in a lattice site, will be separated into neighboring two lattice sites as an antiferromagnetic pair. This antiferromagnetic pair, once generated by the light, will proliferate and will grow up to be a nonequilibrium SDW domain.

To study such a lattice relaxation of CT excitation, we can introduce the following disk type lattice distortion pattern Q_ℓ

$$Q_\ell = (-1)^{\ell_x+\ell_y} Q_0 \left[1 + \Delta Q \{ \tanh[\theta(\sqrt{\ell_x^2 + \ell_y^2} - \ell_D/2)] - 1 \} \right] . \tag{26}$$

Here $(-1)^{\ell_x+\ell_y} Q_0$ denotes the aforementioned Peierls distortion in the true ground state. The second term in the square brackets [...] denotes a local lattice displacement induced by a new excited domain. ΔQ is its amplitude, θ again corresponds to the width of the domain boundary, and ℓ_D is the diameter of the domain, which, in the present case, is assumed to be a disk type in the square lattice. When ΔQ=0.5, it is obvious that lattice inside domain has no distortion at all, while we have already seen in Fig. 28(a) that the SDW false ground state has also no lattice distortion. Hence, the SDW order is expected to appear in this domain

too, if we choose ℓ_D and θ properly.

In the present study, we will not investigate the lattice relaxation process in very detail, but just want to demonstrate a possible relaxation path from the true ground state to the expected SDW domain. Hence, we fix the domain diameter ℓ_D at ℓ_D=10, and describe the adiabatic energy of the ground state E_g only as a function of ΔQ, while θ is determined to minimize the domain energy at T=0. Figure 29 shows the adiabatic energy curve of E_g, which is referenced from the true ground state. If we start from the origin $\Delta Q = 0$, E_g rapidly increases up to 0.9 eV, and after that it turns to go down to another minimum near $\Delta Q = 0.5$. Thus, this minimum is locally stable, and has the SDW order. To elucidate the nature of this domain, we present its lattice distortion pattern Q_ℓ and spin density pattern in Fig. 30. The diameter of each dot in Fig. 30(a) is proportional to $|Q_\ell/Q_0|$, while the diameter of each dot in Fig. 30(b) is proportional to $|<n_{\ell,\alpha}> - <n_{\ell,\beta}>|$, at each lattice site. The value of $|<n_{\ell,\alpha}> - <n_{\ell,\beta}>|$ at the center of the domain is almost equal to that of Fig.28(a). It is now clear that this local domain exhibits the SDW order just as we have expected, and it can be generated by the photoexcitation at low enough temperature. By the dotted and dashed lines in Fig 29, we have schematically shown a possible relaxation path of the CT excitation from the CDW ground state to this SDW domain. Although this photoinduced phase may not have a long lifetime, there is no fundamental difficulty to detect it by using modern spectroscopy techniques.

Thus, through the photoinduced nonequilibrium phase, we can recognize the presence of an interaction H_n and its resultant broken symmetry, even if it is almost completely hidden in any equilibrium phases from absolute zero temperature to high ones.

Let us now consider this conclusion from a more general point of view. Real solids are so complex that, although they are made of only a few kinds of atoms and molecules, their structures show great number of variations under different chemical and physical environments, and are stabilized by delicately balanced interactions. It is far from rare that an interaction, being only a little weaker than its counterparts, can really appear under very limited conditions. In many cases, it just disappears from our scope of study, simply because its strength is subsidiary than other more dominant counterparts. Therefore it is vitally important to elucidate such a new interaction and its resultant broken symmetry by a photoinduced nonequilibrium phase.

7.6 Hysteresis and nonadiabatic effect

Let us qualitatively discuss the effect of hysteresis in connection with nonadibabatic effects coming from the fourth term of eq.(20). The CDW-metal transition shown in Fig.27 is the first order phase transition, and hence we have to expect the following hysteresis effects around T_c. Slowly warming the whole system from low temperature to high one across T_c, we can make the CDW state remain even above T_c as a locally stable nonequilibrium state, whose free energy is higher than the globally stable (equilibrium) metallic state. This situation is also same for the cooling process from above T_c, and the difference between the warming process and the cooling one is usually called hysteresis loop. The region of temperature in which this hysteresis phenomena occur is mainly determined by the nonadiabatic effects coming from the fourth term of eq.(20). When the energy difference between the nonequilibrium state and the globally stable

equilibrium one becomes large, a nonadiabatic (or diabatic) transition will surely occur from this nonequilibrium state to this equilibrium one, provided that M is large but finite.

In this context, the aforementioned hysteresis phenomena can be understood as the following situation, that these two states are almost degenerated with each other, and hence, the life time of the aforementioned decay transition becomes quite long as compared with the time scale of our daily life. Thus the nonequilibrium state due to the hysteresis effect can appear only in the vicinity of T_c.

While, the photoinduced nonequilibrium state mentioned before can appear even outside of this hysteresis loop, although its life time is often shorter than the time scale of our daily life. As mentioned before, according to the recent progress of our laser spectroscopy techniques, an infinite life time is not necessary for each state to be recognized as a well-defined state, provided that can last long enough to be clearly observed by other photons to detect it.

8. Photoinduced macroscopic parity violation and ferroelectricity

In previous sections, we have been concerned with various photoinduced structural phase transitions, which, after the complicated nonlinear lattice relaxation, finally result in false ground states. These states are, of course, no more luminescent, as schematically shown in Fig.1. However, by recently experimental studies on $SrTiO_3$, we have discovered a new type photoinduced structural phase transition, which occurs only within the optical excited state, keeping this state still luminescent. In these materials, a photogenerated conduction electron results in a ferro-(or super-para-) electric domain with a macroscopic parity violation.

8.1 Large polaron, self-trapped polaron, linear and quadratic couplings

An electron, excited from a valence band to a conduction one by a photon in an insulating solid, often forms a quasi-particle called polaron, being composed of the original electron and the phonon cloud around itself. This polaron effect, coming from the interaction of the electron with phonons or lattice vibrations, has been a matter of considerable interests for these 40 years, and many experimental and theoretical studies have already been devoted. It is one of most basic themata related with various fields of the solid state physics, such as optics and electronic conductivities in many kinds of semiconductors and insulators[33,34,35].

At present, it is well-known, that this polaron can be clearly classified into two types, the large polaron and the self-trapped one, provide that the electron-phonon (e-p) interaction is short ranged in ordinary three dimensional crystals.[34] These two different types are brought about through the competition between the quantum itineracy of electron and the strength of e-p coupling.

When the e-p coupling is weak as compared with the itineracy, or the energy-band width of this conducting electron, we can get the large (or free) polaron, extending over a wide region of the crystal. In this case, the phonon cloud or the lattice distortion cloud around the electron, has a large radius as compared with the lattice constant of this crystal. While, the thickness of this cloud is rather thin, because of the weakness of this e-p coupling. These large polarons, once formed in a crystal by photoexcitations, can greatly contribute to increase the photoconductivity or the electronic conductivity. On the other hand, when the e-p coupling is strong as compare with the energy-band width, the electron, self-induces a potential well of local lattice distortion only around a single lattice site of the crystal, and is trapped in it. This is the self-trapped (or small) polaron, which never contributes to the ordinary electronic conductivity.

It is also well-established, that these two states, the large and self-trapped polaron states, are clearly separated by an energy barrier in the adiabatic potential surface, just like the first order phase transitions. Hence, the large polaron state can remain as a locally stable state in the adiabatic potential surface, even when the e-p coupling is strong enough to make the self-trapped state globally stable.[34] However, in this competition between the large polaron and self-trapped one, the original e-p coupling is tacitly assumed to be

linear and short ranged. That is, a local electron density at a certain position only linearly couples with a phonon field of the same position through a contact interaction. Consequently, if the original crystal lattice has a space inversion symmetry, only the phonon mode with even parity can contribute to this coupling, and possible contributions coming from odd phonon modes are excluded.

For this reason, in this section, we will see possible contributions coming from odd phonon modes under the condition that our starting crystal lattice has a space inversion symmetry[36]. In this case, the conduction-band electron couples, not linearly, but quadratically with odd mode phonons. The effects of this quadratic coupling have not been seriously taken into account, or often been neglected, because, this quadratic coupling can be easily merged into the original restoring force of this mode, if this force is very strong or hard. However, if this odd mode is quite soft and anharmonic, the quadratic e-p coupling, switched on by the photogeneration of an electron, will result in parity violating instabilities and ferroelectric phase transitions, which are absent in the cases of even modes.

8.2 Photoinduced phenomena in $SrTiO_3$

This problem is closely related with recent optical experiments on the perovskite type $SrTiO_3$ [37,38,39,40].

As shown in Fig.31, the structural unit of this material is an O^{2-} octahedron with a Ti^{4+} ion in its center.[41] The six apices of this octahedron are connected with each other, three dimensionally. The top of the valence band of this material is mainly composed of the 2p orbital of O, and the bottom of the conduction band is mainly composed of the 3d orbital of Ti.[42] In between, there is a wide indirect energy gap of about 3.2eV.[40,42]

Irradiating this wide gap material by ultraviolet light, Yasunaga[37],Takesada et al[38], and Hasegawa et al[39], have very recently found that the electronic conductivity and the quasi-static electric susceptibility are macroscopically enhanced. From the hole coefficient measurements by Yasunaga[37], this increase of the conductivity has been already known to come, not from the holes, but from the electrons. Hence, a pair of the 3d electron and the 2p hole generated by the light, is shown to separate into a mutually independent electron and hole, with no exciton effect in between. After this separation, only the electron remains as a mobile carrier, while the hole is assumed to be trapped and localized by some reason, which is unknown. On the other hand, the quasi-static electric susceptibility, or the real part of the quasi-static dielectric constant ($\equiv \varepsilon_1$), is shown to increases about 10^3, between before and after this irradiation.[38,39]

An extraordinarily long lived luminescence, arising from this irradiation, is also found by Hasegawa et al[40] at 2.4 eV, and the electron and hole are, thus, shown to recombine and disappear. While, this luminescence has a large Stokes shift of about 0.8 eV. It tells us that the electron and hole strongly couples with the phonon mode, which mainly corresponds to the breathing (A_{1g}) type motion of O^{2-}s around Ti^{4+}, and has an energy of about 20 meV.[40] What is very interesting is that, the aforementioned enhancement of ε_1 disappears as this luminescence terminates. It clearly means that this enhancement is directly related to the presence of electron or (and) hole.

8.3 Quantum dielectric, soft-anharmonic T_{1u} mode and quadratic coupling

The perovskite type compound $SrTiO_3$ is well-known as the quantum dielectric, and long before the aforementioned optical studies, many elaborate works have already been systematically devoted to the ground state properties of this material with no photogenerated electron (hole)[43-48]. They are mainly concerned with low temperature properties of ε_1, in relation to soft and anharmonic natures of T_{1u}(TO) mode, which mainly corresponds to an off-center type displacement motion of a Ti^{4+} ion, from the central position of the O^{2-} octahedron. In Fig.32, we have schematically shown the pattern of this T_{1u} mode together with the aforementioned A_{1g} mode. Qualitatively speaking, the Ti^{4+} ion is only loosely confined within this octahedron, and hence, it has a very large quantum fluctuation around the central position. Thus, we can expect to get various parity violating instabilities and ferroelectric phase transitions. However, this material $SrTiO_3$ remains only in the super-para-electric phase down to 0K without global frozen parity violation, being called quantum dielectric with no ferroelectric phase transition.

According to Muller et al[44], this T_{1u} mode has almost no, or even a negative restoring force, if it is described only in terms of this T_{1u} mode coordinate. However, it has an effective positive frequency of about 1 meV, which comes from a quite specific anharmonicity, called "bi-quadratic mode-mode coupling" between this T_{1u} mode and other acoustic phonon modes[44,45]. In many cases of soft-anharmonic phonons, we are often tempted to simply imagine an ordinary single-mode double-well type anharmonicity, composed of a positive quartic potential and a negative quadratic one, only in terms of this site localized T_{1u} phonon coordinate. However, by Muller et al[44] and also by Vogt[46], this type single-mode quartic anharmonicity is completely shown not to be realized in this material at low temperatures, while the single-mode sextic anharmoniocity model is shown to be rather appropriate [46].

By the Raman scattering measurements, this soft T_{1u} phonon is proved to couple not linearly but quadratically with electronic excitations[49], although its coupling strength seems to be one order smaller as compared with the linear coupling of the breathing (A_{1g}) mode. Together with the aforementioned large quantum fluctuation, this quadratic coupling is expected to result in some macroscopic parity violation in the photoexcited states, although it is never realized in the ground state.

8.4 Possible scenario

Let us now proceed to a possible scenario that describes the aforementioned enhancement of the conductivity and ε_1 in the photoexcited state. By a VUV photon irradiation, a conduction electron is generated in the 3d orbital of Ti, and this orbital is making an itinerant energy band with a width of about 2eV, through its hybridization to the 2p orbital of O[42]. This electron linearly and strongly couples with the breathing (A_{1g}) mode of O around the Ti, and hence, as explained before, we have both the metastable large polaron state and the globally stable self-trapped state. Since the large polaron state is energetically higher that the self-trapped one, the photogenerated electron reaches this state first[21]. As explained before, this state can

contribute to the electronic conductivity.

On the other hand, this large polaron state quadratically couples with the T_{1u} phonons, and the sign of this quadratic coupling constant is "negative" for the reason we see later in detail. Thus, the quadratic coupling makes this soft mode more "soft". This further softening due to the e-p coupling occurs at very large number of lattice sites, which are included in this large polaron radius. Since this mode is dipole active, this further softening consequently contributes to the enhancement of quasi-static ε_1.

8.5 Model Hamiltonian

Keeping this scenario in mind, let us start from the following model Hamiltonian ($\equiv H_f$) that describes the electrons in the 3d conduction band of $SrTiO_3$, coupling linearly with the breathing mode, and quadratically with the T_{1u} mode, as, ($\hbar = 1$)

$$H_f = -T_f \sum_{\ell,\ell',\sigma} \{c^+_{\ell,\sigma} c_{\ell',\sigma} + \text{h.c.}\} - S_b \omega_b \sum_{\ell} n_\ell A_\ell + \frac{\omega_b}{2} \sum_{\ell} \left(-\frac{\partial^2}{\partial A^2_\ell} + A^2_\ell \right)$$

$$- \frac{S_d \omega_d}{2} \sum_{\ell,i} n_\ell D^2_{\ell,i} + \frac{\omega_d}{2} \sum_{\ell,i} \left(-\frac{\partial^2}{m \partial D^2_{\ell,i}} + \frac{D^6_{\ell,i}}{3} \right)$$

$$+ U_f \sum_{\ell} n_{\ell,\alpha} n_{\ell,\beta}. \qquad (27)$$

Here, $c^+_{\ell,\sigma}$ is the creation operator of an electron at a lattice site ℓ with spin $\sigma(=\alpha,\beta)$ in a simple cubic crystal, and T_f is the transfer energy between neighboring two lattice sites ℓ and ℓ'. S_b is the dimensionless constant of linear coupling between this electron and the site localized breathing (A_{1g}) mode, whose energy is ω_b and dimensionless coordinate is A_ℓ. On the other hand, $S_d(>0)$ is the dimensionless constant of the quadratic coupling between the electron and the site localized T_{1u} mode, whose energy is ω_d and dimensionless coordinate in the direction i(= x, y, z) is $D_{\ell,i}$. While U_f denotes the intra-site (intra-orbital) Coulomb repulsion. The dispersions of phonons are neglected, and only the long wave characteristics of each mode are taken into account.

The origin of a short range quadratic coupling between a site localized T_{1u} mode and an electron around it, is already well-known to be an off-center effect[50,51]. It comes from the local mixing between the occupied atomic orbital of the electron, and unoccupied ones which are energetically higher than this occupied one but have opposite parities. This mixing is brought about by a linear change of the crystal field

coming from the off-center type T_{1u} displacement of a central atom. Within the second order perturbation theory, the resultant energy change ($\equiv \Delta E$) of the occupied state is given as

$$\Delta E = - D^2 \sum_j \frac{< o | V | j >< j | V | o >}{E_{jo}}, \qquad (28)$$

where, $|o>$ and $|j>$ denote occupied and unoccupied atomic orbitals, whose parities are opposite each other, and E_{jo} is the energy difference between them. V is an electronic operator with T_{1u} symmetry, and denotes the linear change of the crystal field due to the T_{1u} type displacement D, whose site and direction indices ℓ and i are omitted. We can see that ΔE is always negative as far as $|o>$ is the highest occupied atomic orbital. Thus, we can get a negative quadratic interaction, and it is a driving force for the central atom to push off its original position[51]. We should note that this "off-center" effect is nothing but the local parity violation, resulting in a local and microscopic ferroelectricity.

In the present case, the Wannier function of the conduction band electron is mainly composed of the 3d orbital of Ti, hybridized with the 2p orbitals of O. This Wannier function mixes with the 4p orbital of Ti and the 3s orbital of O due to the T_{1u} type off-center displacement of the central Ti ion. In addition to these typical atomic orbitals, there are many other unoccupied higher electronic states, that can locally mix with the Wannier function. Thus, we can get a negative quadratic coupling as described by the fourth term of eq.(27), wherein S_d only phenomenologically represents the effects of all aforementioned local mixings. The typical energy difference E_{jo} is about 10 eV, and hence this off-center effect is usually neglected. As mentioned before, if the original restoring force of this mode is very strong or hard, this quadratic coupling can be easily merged into this original hard force. However, in the cases of soft-anharmonic modes, the quadratic coupling becomes very important in connection with parity violating instabilities, even though it is not strong.

It should be noted that, our purpose in the present section, is not to estimate this coupling energy S_d quantitatively. Our purpose is to clarify possible parity violations coming from this quadratic e-p coupling, under the condition that this effect is one order smaller, than both the itineracy of the electron and the linear e-p coupling.

As for the anharmonicity of the fifth term of eq.(27), we have taken a sextic one, for the reason mentioned before in detail. While "m" in this fifth term, denotes the dimensionless effective mass of this site localized T_{1u} mode. This mass will be determined so that the lowest vibronic excitation energy of this soft-anharmonic Hamiltonian becomes equal to ω_d, which is obtained by the experiment[45].

We now rewrite H_f into the following dimensionless form as

$$h \equiv H_f / \omega_b = -t \sum_{\ell,\ell',\sigma} \{c^+_{\ell,\sigma}\, c_{\ell',\sigma} + \text{h.c.}\} + u \sum_{\ell} n_{\ell,\alpha}\, n_{\ell,\beta}$$

$$- s_b \sum_{\ell} n_\ell a_\ell + \frac{s_b}{2} \sum_{\ell} a^2_\ell - \frac{1}{2 s_b} \sum_{\ell} \frac{\partial^2}{\partial a^2_\ell}$$

$$- \frac{\gamma s_d}{2} \sum_{\ell,i} n_\ell\, d^2_{\ell,i} + \frac{\gamma s_d}{6} \sum_{\ell,i} d^6_{\ell,i} - \frac{\gamma}{2 m s_d^{1/3}} \sum_{\ell,i} \frac{\partial^2}{\partial d^2_{\ell,i}}\,, \tag{29}$$

where

$$t \equiv T_f / \omega_b,\ u \equiv U_f / \omega_b,\ s_b \equiv (S_b)^2,\ \gamma \equiv \omega_d / \omega_b,\ s_d \equiv (S_d)^{3/2},$$
$$a_\ell \equiv s_b^{-1/2}\ A_\ell,\ d_{\ell,i} \equiv s_d^{-1/6}\ D_{\ell,i}\,. \tag{30}$$

Assuming t, u, s_b, s_d are all greater than unity

$$(t,\ u,\ s_b,\ s_d) \gg 1, \tag{31}$$

we can define an adiabatic Hamiltonian h_{ad} as

$$h \to h_{ad} \equiv -t \sum_{\ell,\ell',\sigma} \{c^+_{\ell,\sigma}\, c_{\ell',\sigma} + \text{h.c.}\} + u \sum_{\ell} n_{\ell,\alpha}\, n_{\ell,\beta} - s_b \sum_{\ell} n_\ell a_\ell + \frac{s_b}{2} \sum_{\ell} a^2_\ell$$
$$- \frac{\gamma s_d}{2} \sum_{\ell,i} n_\ell\, d^2_{\ell,i} + \frac{\gamma s_d}{6} \sum_{\ell,i} d^6_{\ell,i}\,. \tag{32}$$

8.6 Variational method for polaron

Let us now proceed to a variational calculation for a polaron. For this single polaron state $|p>$ we use a trial function $(\equiv \varphi(\ell))$ as,

$$|p> \equiv \sum_{\ell} \varphi(\ell)\, c^+_{\ell,\alpha}\, |0>>, \quad \sum_{\ell} |\varphi(\ell)|^2 = 1, \tag{33}$$

where $|0>>$ is the true electron vacuum. After taking the expectation value of h_{ad} with respect to this

$|\,p>$, we get

$$< h_{ad} >=< -t \sum_{\ell,\ell',\sigma} \{ \ldots \} > - s_b \sum_{\ell} < n_{\ell,\alpha} > a_\ell + \frac{s_b}{2} \sum_{\ell} a_\ell^2 - \frac{\gamma s_d}{2} \sum_{\ell,i} < n_{\ell,\alpha} > d_{\ell,i}^2$$

$$+ \frac{\gamma s_d}{6} \sum_{\ell,i} d_{\ell,i}^6 , \qquad < \ldots\ldots > \equiv < p \,|\, \ldots\ldots \,|\, p >. \tag{34}$$

By the Hellman-Feynman theorem, we obtain as

$$\frac{\partial < h_{ad} >}{\partial a_\ell} = 0, \rightarrow < n_{\ell,\alpha} > = a_\ell, \quad \frac{\partial < h_{ad} >}{\partial d_{\ell,i}} = 0, \rightarrow < n_{\ell,\alpha} >^{1/4} = d_{\ell,i}. \tag{35}$$

Substituting this eq.(35) into eq.(34), we finally get

$$< h_{ad} >=< -t \sum_{\ell,\ell',\sigma} \{ \ldots \} > - \frac{s_b}{2} \sum_{\ell} < n_{\ell,\alpha} >^2 - \frac{\gamma s_d}{3} \sum_{\ell,i} < n_{\ell,\alpha} >^{3/2} . \tag{36}$$

8.7 Continuum approximation and super-paraelectric large polaron

Let us take the following Gaussian type trial function with a reciprocal localization length ($\equiv \Delta_p$) as

$$\varphi(\ell) \propto \exp[-\frac{\Delta_p^2 (\ell \cdot \ell)}{2}], \quad \ell = (\ell_x, \ell_y, \ell_z), \tag{37}$$

where ℓ_x, ℓ_y and ℓ_z are the Cartesian components of ℓ. Using the continuum approximation, we regard ℓ_i ($i = x, y, z$) as a continuous variable from $-\infty$ to ∞. In this case, the first term of eq.(36) is reduced as

$$< -t \sum_{\ell,\ell',\sigma} \{ \ldots \} > \rightarrow \int_{-\infty}^{\infty} d\ell_x \int_{-\infty}^{\infty} d\ell_y \int_{-\infty}^{\infty} d\ell_z \varphi(\ell) \left[-t \left(\frac{\partial^2}{\partial \ell_x^2} + \frac{\partial^2}{\partial \ell_y^2} + \frac{\partial^2}{\partial \ell_z^2} \right) \right] \varphi(\ell), \tag{38}$$

wherein, all the one-body energies are referenced from the bottom of the conduction band. Other two terms in eq.(36) can be easily calculated within this continuum approximation, and we finally get as,

$$< h_{ad} > = \frac{3 t \Delta_p^2}{2} - \frac{s_b \Delta_p^3}{2^{5/2} \pi^{3/2}} - \frac{2^{5/2} (\gamma s_d) \Delta_p^{3/2}}{3^{3/2} \pi^{3/4}}. \qquad (39)$$

Before we go in detail about the numerical results calculated by using this eq.(39), let us qualitatively examine energetics of $< h_{ad} >$. It is shown in Fig.33 as a function of Δ_p. When $(\gamma s_d) = 0$, the first term of $< h_{ad} >$, being the kinetic energy, increases in proportion to Δ_p^2, while, the second term, being the energy gain due to the self-trapping by the breathing (A_{1g}) mode, decreases in proportion to $-\Delta_p^3$, as shown in Fig.33(a). If these two competing quantities are of the same order, we get two minima of $< h_{ad} >$. The minimum at $\Delta_p = 0$ in Fig.33(a), denotes the well-known large (or free) polaron, while the other minimum at large Δ_p, being not written explicitly, is the self-trapped (small) polaron. It should be noted that all these states have even parities irrespective of Δ_p. As mentioned before, these two states are separated by an adiabatic energy barrier, and hence, the large polaron state can be locally stable, even when the self-trapped polaron state is globally stable[33,34].

When $(\gamma s_d) \neq 0$, however, the energy gain due to the T_{1u} type parity violation is proportional to $-\Delta_p^{3/2}$, being most dominant in the small limit of Δ_p as shown in Fig.33(b). Hence the previous minimum at $\Delta_p = 0$ now moves to a small but finite Δ_p. Thus, we can get a very important conclusion within the adiabatic approximation. An infinitesimal (γs_d) is enough to change the even-parity large polaron into the parity violating one, although the energy gain due to this symmetry breaking is quite small. This parity violation occurs at a large number of lattice sites included in the large polaron radius, and hence it is a quasi-global parity violation, as schematically shown in Fig.34. While, the self-trapped state, being not written explicitly in Fig.33(b), also has a parity violation, but it is quite local. Hence, we can call it the off-center type self-trapped state, wherein only the central atom will move off the original position, as shown in Fig.30. This off-center effect will be rather slight, since the lattice distortion of this state is mainly dominated by the strong coupling of the breathing mode.

It should be also noted that this parity violation of the T_{1u} mode is tacitly accompanied by the parity violation of the Wannier function itself, as mentioned in eq.(28). Originally, this function has T_{2g} or E_g symmetry of the O_h point group, since it is the 3d orbital of Ti. However, as the T_{1u} type off-center displacement occurs, it mixes with unoccupied T_{1u} type atomic orbitals, resulting in a finite dipole, and the parity violation in the electronic level too, although this change is hidden.

It is also very essential, that the phase of this local parity violation is quite random, and has no inter-site coherence, since phonons are site-localized ones, and the quadratic coupling is also independent of this phase. However, a weak external electric field may be enough to make it spatially coherent, as schematically shown in Fig.34. In this sense, our new large polaron is super-pare-electric(SPE) one, which

has a quasi-global parity violation. It is essentially same as a charged and conductive ferroelectric domain.

Let us now examine the nature of the anharmonicity used in this theory. For the reason mentioned above in detail, the sextic anharmonicity is used in eq.(27). In this sextic case, an infinitesimal γs_d is enough for the parity violation to occur. However, even if we change this sextic anharmonicity to other ones higher than quintic as,

$$\frac{\omega_d}{2}\sum_{\ell,i}\frac{D_{\ell,i}^6}{3} \rightarrow \frac{\omega_d}{2}\sum_{\ell,i}\frac{|D_{\ell,i}^{2M}|}{M}, \quad M > 2.5, \qquad (40)$$

we can also easily prove the occurrence of the same adiabatic instability for an infinitesimal γs_d. While, in the case of the aforementioned single-mode quartic double-well, the instability already occurs in the ground state itself, and hence, the photogenerated electron may not induce further instabilities.

8.8 Numerical results

Keeping these general characteristics in mind, let us see results of further numerical calculations. According the quantum chemical theory by using a small cluster model for various perovskite type metal-oxides, the binding energy of the self-trapped poralon is shown to be few times of 0.1eV[52], which is much smaller that the aforementioned conduction band width (2eV) or the energy gap (3.2eV). Hence, we can say that, in this type compound family, the self-trapping is marginal, in the sense that the itineracy and the e-p coupling are well balanced. We, hereafter, will be concerned only with this marginal case.

In order to describe this marginal situation in the context of the present continuum approximation, we, at first, have to determine the meaningful maximum of Δ_p. For this maximum, we use $\Delta_p \leq 2$. The present continuum model has no meaning for too large Δ_ps, and this limit $\Delta_p = 2$ is determined, since $|\varphi(\ell)|^2$ at $\ell = (1,0,0)$ becomes almost zero for larger Δ_ps than 2. Using this maximum value $\Delta_p = 2$, and neglecting the effects of the T_{1u} mode in eq.(39), we get the marginal condition for s_b as,

$$6\,t \leq \frac{\sqrt{2}\,s_b}{\pi^{3/2}}. \qquad (41)$$

Since, $12\,T_f$ = 2eV, t becomes t = 8.33. In this case, the marginal s_b is given as $s_b \geq 200$. Under this condition the self-trapped state becomes the globally stable one. While, from the following equation for Δ_p,

$$\frac{\partial < h_{ad} >}{\partial \Delta_p} = 0, \rightarrow \frac{s_b \Delta_p^{3/2}}{2^{5/2}\pi^{3/2}} - t\Delta_p^{1/2} + \left(\frac{2}{3}\right)^{3/2}\frac{(\gamma s_d)}{\pi^{3/4}} = 0, \qquad (42)$$

we can derived the condition to make the SPE large polaron locally stable. If this equation for Δ_p gives two roots in the region $0 < \Delta_p < 2$, the large polaron becomes locally stable in the adiabatic potential surface,

just as schematically shown in Fig.29(b). Regarding this eq.(42) as a cubic equation with respect to $\Delta_p^{1/2}$, we get this condition as,

$$(\gamma s_d)^2 < \frac{(\sqrt{2}\pi t)^3}{s_b} \quad . \qquad (43)$$

When t=8.33 and $s_b = 200$, it becomes, $\gamma s_d < 15.9$.

As mentioned before, our purpose in the present section is not to estimate this quadratic coupling constant γs_d quantitatively. Our purpose is to clarify possible parity violating instabilities coming from this quadratic e-p coupling, under the condition that this coupling is one order smaller that both the itineracy and the linear e-p coupling. In Fig.35, we have shown one of such typical cases. It is obtained by the following set of parameters, ω_b =20meV, t=8.33, $s_b = 200$, $\gamma = 0.05$, $\gamma s_d = 15$. The resultant SPE large polaron extends over about 1000 lattice sits, and its binding energy is far smaller than ω_b. While, the self-trapped state has a binding energy of about $20\,\omega_b$, although it is not written explicitly in this Fig. 35. Throughout this review paper, we will not be concerned with quantitative calculations for the electronic conductivity. However, we can say, that this SPE large polaron (or this charged ferroelectric domain) is far mobile than the self-trapped state, and can surely contribute to the increase of the conductivity.

8.9 Singlet bipolaron

Let us now proceed to the next problem whether phogenerated neighboring two electrons can make a stable singlet bipolaron, as compared with independent two polarons. For a singlet bipolaron state ($\equiv |\mathrm{bp}>$), we use a trial function ($\equiv \varphi_b(\ell)$) as,

$$|\,\mathrm{bp}> \equiv \sum_{\ell,\ell'} \varphi_b(\ell)\,\varphi_b(\ell')\,a^+_{\ell,\alpha}\,a^+_{\ell',\beta}\,|0>> \,, \quad \sum_{\ell} |\varphi_b(\ell)|^2 = 1,$$

$$\varphi_b(\ell) \propto \exp\{-\Delta_b^2(\ell\cdot\ell)/2\}, \qquad (44)$$

where, Δ_b is the reciprocal localization length of this bipolaron. By the same method used before, we can get the energy per electron as

$$\frac{<\mathrm{bp}\,|h_{ad}\,|\,\mathrm{bp}>}{2} = \frac{3t\Delta_b^2}{2} - (s_b - \frac{u}{2})\frac{\Delta_b^3}{2^{3/2}\pi^{3/2}} - \frac{8(\gamma s_d)\Delta_b^{3/2}}{3^{3/2}\pi^{3/4}} \quad . \qquad (45)$$

Since this system is based on the 3d orbital of Ti, the inter-electron Coulomb repulsion is stronger than both the itineracy and the linear e-p coupling, and hence the self-trapped bipolaron seems to be unstable. However,

the large bipolaron will be stable enough, since its mean inter-electron distance is very large. As one of typical examples for such cases, we take $u/s_b = 1.75$, keeping other parameters same as before, and can get the result shown in Fig.35.

We can see that the SPE large bipolaron is stable relative to the two separated SPE polarons, while the self trapped bipolaron is unstable. From Fig.35, we can also see that the SPE large bipolaron can fissure into isolated two self-trapped polarons, through a quantum tunneling process, as schematically shown by a dashed allow. This may be a rather slow process, since the localization radius of the polarons has to change largely and almost discontinuously between initial and final states of this tunneling[53].

8.10 Further softening and enhanced ε_1

Let us now proceed to the aforementioned further softening of the T_{1u} mode and the enhancement of ε_1. At first, we will reconfirm the original soft-anharmonic nature of the T_{1u} mode at the ground state. It is given only by the fifth term of eq.(27) without the electron. By using a variational method, we determine the lowest vibronic state $(\equiv|+>)$ and its energy$(\equiv E_+)$ at site ℓ and in the direction i, as well as those $(\equiv|->,\ \equiv E_-)$ of the second lowest state. Hence, we use the following trial functions

$$|+> \propto \exp\{-(\kappa_+ D)^2/2\}, \qquad |-> \propto D \exp\{-(\kappa_- D)^2/2\}, \tag{46}$$

where $\kappa_\pm$ is the variational parameter of $(\equiv|\pm>)$, and the indices ℓ and i of D are omitted. After the variational calculation, we get $\kappa_+ = 1.2253$, $E_+/\omega_d = 0.3693$, $\kappa_- = 1.3622$, $E_-/\omega_d = 1.3693$, and these energies are referenced from the minimum point of the sextic potential $D=0$. Since we have used $m = 1.3351$, the lowest excitation becomes $(E_- - E_+)/\omega_d = 1$, as shown in Fig.36(a).

Let us roughly estimate the further softening due to the aforementioned negative quadratic e-p interaction. By this interaction, the effective potential at each lattice site will become a double well type one as schematically shown in Fig.36(b). Exactly speaking, the T_{1u} type motions of Ti ions are now not mutually independent, but are correlated with each other, since they are coupling to the same electron which is not localized. In order to avoid this complexity, we focus only on a single mode at a typical lattice site, for example, the x direction of the central site of the bipolaron, and fix all the coordinates of other modes at the values determined by the previous adiabatic and variational method, eq.s (44) and (45). Then, we can get an effective Hamiltonian $(\equiv H_{ef})$ only for this mode as,

$$H_{ef} = -S_d \omega_d |\varphi_b(0)|^2 D^2 + \frac{\omega_d}{2}\left(-\frac{\partial^2}{m\,\partial D^2} + \frac{D^6}{3}\right). \tag{47}$$

It gives a new double well potential with two minima at $D = \pm D_0$

$$D_0 \equiv \left(2 S_d \mid \varphi_b(0) \mid^2\right)^{1/4} . \qquad (48)$$

The electronic state $\varphi_b(0)$ may depend also on D of this mode. However, this electron is extended over about 1000 lattice sites, and hence we can neglect it. Using this H_e, we can determine the lowest vibronic excitation energy by using the following variational method.

$$|\pm>' \propto \{ \exp[-\kappa'_{\pm}(D-D_0)^2/2] \pm \exp[-\kappa'_{\pm}(D+D_0)^2/2] \}, \quad (49)$$

where $|\pm>'$ denotes the lowest (second lowest) state with a variational parameter $(\equiv \kappa'_{\pm})$ and an energy $(\equiv E'_{\pm})$. Using the result shown in Fig.35, we get $\kappa'_{+} = 1.760$, $E'_{+}/\omega_d = 0.977$, $\kappa'_{-} = 2.010$, $E'_{-}/\omega_d = 1.232$, and these energies are referenced from the minimum point $D = D_0$ in Fig.36(b). Thus, the lowest excitation energy $(\equiv \omega')$ is given as $\omega' = (E'_{-} - E'_{+}) = 0.255\,\omega_d$, and we have finally gotten the further softening. We can say that, after the photoexcitation, the original vibronic wave function shown in Fig.36(a), bifurcates as shown in Fig.36 (b). The lowest excitation energy decreases into about 1/4 of the original, because of this bifurcation.

From this further softening, we can roughly estimate the enhancement of ε_1. The matrix element of the dipole transition in this T_{1u} mode will not be changed so much in spite of this bifurcation. Under this condition the relative change of the quasi static dielectric constant is roughly estimated as

$$\frac{(\text{relative change of } \varepsilon_1)}{(\text{polaron density})} = \frac{(\text{polaron volume})}{(\omega'_d / \omega_d)}, \quad (50)$$

wherein the polaron density itself varies depending on the exciting light intensity of each experiment. While, the polaron volume can be roughly estimated from the values of Δ_p and Δ_b shown in Fig.35. Thus, by the present theory, we can conclude that the enhancement factor is just the right hand side of eq.(50). It is concluded to be of the order of 10^4.

As mentioned before, this is also a kind of photoinduced structural phase transition, occurred in the optical excited state, and we can finally get a charged and conductive ferroelectric domain.

9. Photoinduced structural phase transitions observed by x-ray measurements

As mentioned occasionally in previous sections, the most simple and standard technique to observe the photoinduced phase transitions is the so-called modulation spectroscopy, in which another visible photon is

shone to detect spectroscopic changes between before and after the transition. Although this method was proved to be quite useful, it is rather indirect to observe structural changes of the crystal lattice. Very recently, however, we have succeeded to observe the PSPT's more directly, using the time resolved x-ray structure analysis. This direct measurement is fulfilled in TTF-CA by Siders et al[54], and also by Collet et al[55], independently. The aforementioned structural difference between the photoinduced phase and the thermally induced one in the organo-metallic complex crystal is also directly observed by Moritomo et al[56], through the x-ray structure analysis.

While, very recently, Nozawa et al[57] have succeeded to observe the photoinduced macroscopic parity violation in $SrTiO_3$, using the x-ray inner core absorption spectroscopy. The 1s-3d inner core transition of the Ti ion, having an energy of about 4968eV, is dipole forbidden, if this ion is exactly at the centre of the octahedron (Fig.31). However, it becomes dipole allowed partially, if the aforementiond off-center type displacement occurs. In this connection, they observed a macroscopic increase of this transition intensity between before and after the VUV light irradiation.

10. Other problems in photoinduced phase transitions

The history of photoinduced phase transition research is quite young, and we have various other problems, which are very important but are not referred in preceding sections.

As for the theoretical models for the photoinduced phase transitions, here, we have been concerned only with the so-called itinerant models, in which the electrons or the excitons are itinerant from site to site. In this connection, Koshino, Ogawa and Sakai[58,59] have developed quite unique theories based on a site-localized two level system (ground and excited states), interacting with other site ones through a classical spring constant. They call it "domino theory", since in this model, a site-localized electronic excitation can proliferate through the spring constant just like the domino game. This theory could successfully describe the photoinduced collective phenomena of the previous organo-metallic complex crystal.

In the previous sections, we have been concerned only with the PSPT, which involves some change of the lattice structural. However, there are various other cases, such as photoinduced magnetic phase transitions[60] and the photoinduced superfluid transitions of high density excitons[61-63], in which, phase transitions or order formations occur only in the electronic degree of freedoms, without the structural change of the lattice.

11. Epilogue, - Where our true ground state comes from -

Thus, we have reviewed the various photoinduced phase transitions. The starting assumption shown in Fig.1 is that, we have our true ground state, which is absolutely stable, or its lifetime is infinitely long. Shining a few visible photons on to it, we can get a macroscopic photoinduced phase. This photoinduced phase can be an entirely new one different from any other existing equilibrium phases. In some case, this photoinduced phase may have a longer lifetime even as compared with the time scale of our daily life. In such a case, this false ground state becomes effectively same as our true ground state, or we cannot practically distinguish which is the true one.

This situation leads us to a more basic question, that is, where our true ground state comes from. The standard text book[64] for the early universe tells us, even our true ground state is also brought about through a kind of phase transition from a photon-dominated universe to a material-dominated one, at the time of the "big barn". The present photoinduced phase transition study again opens the new conversion pathway between photons and materials, whose historical origin is same.

Acknowledgements

The author is very grateful to Professors K.Tanaka, S.Koshihara, K.Yonemitsu, T.Iwazumi, Y.Moritomo and Doctor T. Ishikawa for presenting their research results prior to publication. This work was supported by NAREGI Nanoscience Project, Ministry of Education, Culture, Sports, Science and Technology, Japan.

References

[1] M.Ueta, H.Kanzaki, K.Kobayashi, Y.Toyozawa and E.Hanamura, Excitonic Processes in Solids (Springer-Verlag, Berlin, 1986), p.203.
[2] K.Nasu, Relaxations of Excited States and Photoinduced Structural Phase Transitions, (Springer-Verlag, Berlin, 1997).
[3]K.Nasu, Photoinduced Phase Transitions and Their Precursor Phenomena, Phase Transitions 74 (Gordon Breach, Oxford, 2001), K.Nasu,K.Tanimura,T.Ogawa and A.Nakamura, Photoinduced Phase Transitions, Their Dynamics and Precursor Phenomena, Phase Transitions 75B (Gordon Breach, Oxford, 2002).
[4]K.Nasu, P.Huai and H.Mizouchi, J.P.CM.13 (2001) R693.
[5] K.Nasu , Photoinduced Phase Transitions, (World Scientific, Singapore, 2004).
[6] C.Kittle, Introduction to Solid State Physics, Seventh edition (John Wiley, New York,1996), p. 53.
[7] Y.Tokura,T.Koda,T.Mitani and G.Saito, Solid State Commun. 43 (1982) 757.
[8] S.Koshihara, H.Takahashi, H.Sakai, Y.Tokura and T.Luty, J. Phys. Chem. B 103 (1999) 2592.
[9] T.Suzuki, T.Sakamaki, K.Tanimura, S.Koshihara and Y.Tokura, Phys.Rev.B 60(1999) 6191.
[10] J.Thompson and H.Stewart, Nonlinear Dynamics and Chaos, (John Wiley, New York, 2002), p. 3.
[11] P.Huai, H.Zheng and K.Nasu, J.Phys.Soc.Jpn. 69 (2000) 1788.
[12] M.Cointe, M.Cailleau, H.Cailleau, B.Toudic, L.Toupet, G.Heger, F.Moussa, P.Schweiss, K.Kraft, and N.Karl, Phys. Rev. B 51(1995)3374.
[13] Z.Soos, Annual Review of Physical Chemistry 25 (1974)121.
[14] T.Sakano and Y.Toyozawa, J.Phys.Soc.Jpn.65(1996) 671; Relaxations of Excited States and Photoinduced Structural Phase Transitions, ed K.Nasu (Berlin, Springer-Verlag ,1997), p.160;
[15] W.Su, J.Schrieffer and A.Heeger, Phys.Rev.B 22 (1980) 2099.
[16] N.Nagaosa, J.Phys.Soc.Jpn.55(1986) 2754.
[17] H.Hayashi and K.Nasu, Phys.Rev.B 32 (1985) 5295.
[18] C.Katan, C.Koenig and P.Blochl, Solid State Commun. 102 (1997) 589.
[19] C.Jacobsen and J.Torrance, J. Chem. Phys. 78 (1983)112.
[20] S.Iwai, S.Tanaka, K.Fujinuma, H.Kishida, H.Okamoto and Y.Tokura, Phys. Rev. Letters. 88 (2002) 057402.
[21] K.Nasu, Electron Conduction in Oxides, ed N.Tsuda (Springer-Verlag, Berlin,2000), p.107.
[22] N.Tomita and K.Nasu, Phys. Rev. B 63(2001) 085107.
[23] N.Tomita and K.Nasu, Phys.Rev.B 64 (2001) 125118.
[24] K.Yonemitsu, J.Phys.Soc.Jpn. 73 (2004) 2868-2893.
[25] H.Mizouchi and K.Nasu, J. Phys. Soc. Jpn. 69(2000) 1543.
[26] H.Mizouchi and K.Nasu, J. Phys. Soc. Jpn. 70(2001) 2175.
[27] R.Yabuki and K.Nasu, AIP Conference Proceedings 634 (2002), "Science of Superstrong Field Interactions", ed.by K. Nakajima, p. 362; Synthetic Metals. 135-136 (2003) 705; Physics Letters A 320(2004)286.
[28] R.S.Knox, Theory of Excitons (Academic Press, New York and London, 1963)
[29] J.Feder, FRACTALS (Plenum Press, New York and London, 1988).
[30] Y.Ogawa, S.Koshihara, K.Koshino, T.Ogawa., C.Urano and H.Takagi,Rhys.Rev.Lett.84(2000)3181.

[31] T.Tayagaki and K.Tanaka, Phys.Rev.Letters.86 (2001)2886.
[32] P.Huai and K.Nasu, J.Phys.Soc.Jpn. 71(2002) 1182.
[33] Y.Toyozawa, Polarons and Excitons, ed. by C. Kuper (Oliver and Boyd, Edinburgh,1963), p.211.
[34] Y. Shinozuka and Y. Toyozawa, J.Phys.Soc.Jpn. 46(1989)505.
[35] G. Mahan, Many Particle Physics, (Kluwer Academic, New York, 2000).
[36] K.Nasu, Phys. Rev. B 67 (2003) 174111.
[37] H.Yasunaga, J.Phys.Soc.Jpn. 24 (1968)1035.
[38] M. Takesada, T. Yagi, M. Itoh and S. Koshihara, J.Phys.Soc.Jpn. 72(2003) 37.
[39] T. Hasegawa, S. Mouri, Y. Yamada and K. Tanaka, J.Phys.Soc.Jpn. 72(2003) 41.
[40] T. Hasegawa, M. Shirai and K. Tanaka, Journal of Lumine. 87-89 (2000)1217.
[41] N. Tsuda, Electronic Conduction in Oxides, ed by N. Tsuda (Springer, Berlin, 2000), p. 47.
[42] L. Mattheiss, Phys. Rev. B 6 (1972) 4718.
[43] R.Cohen, Fundamental Physics of Ferroelectrics 2000, AIP CP535 (AIP, New York,2000).
[44] K. Muller and H. Burkard, Phys. Rev. B 19 (1979) 3593.
[45] R. Migoni, H. Bilz and D. Bauerle, Phys. Rev. Letters 37 (1976) 1155.
[46] H.Vogt, Phys. Rev.B 51 (1995) 8046.
[47] V. Fridkin, Ferroelectric Semiconductors, (Consultants Bureau, Plenum, Yew York, 1980).
[48] G. Shirane and Y. Yamada, Phys. Rev. 177 (1969)858.
[49] T. Sekine, K. Uchinokura and E. Matsuura, Solid State Comm. 18 (1976) 569.
[50] F. Luty, Physics of Color Centers, ed. by W. Fowler, (Academic Press, New York, 1986), p.181.
[51] Y.Toyozawa, Optical Processes in Solids, (Cambrigde University, Cambrigde, 2003), p.326.
[52] R. Eglitis, E. Kotomin and G. Borstel, J. Phys. CM 14 (2002) 3735.
[53] K. Nasu and Y. Toyozawa, J.Phys.Soc.Jpn. 50 (1981) 235.
[54] C.Siders and A.Cavalleri, Science 300(2003)592; A.Cavalleri, C.Blome, R.Forget, J.Kieffer, S.Magnan, C.Siders, K.S.Tinten, J.Squier, C.Toth and D. Linde, Phase transitions (Taylor&Francis), 75(2002)769.
[55] E.Collet, M.Cailleau, M.Cointe, H.Cailleau, M.Wulff, T.Luty, S.Koshihara, M.Meyer, L.Toupet, P.Rabiller and S.Techert, Science 300(2003)612.
[56] Y.Moritomo, K.Kato, A.Kurita, A.Nakamoto, N.Kojima, M.Takata and M.Sakata, J.Phys.Soc.Jpn. 71(2002)2609.
[57] S.Nozawa, H.Osawa and T.Iwazumi, Phys.Rev. B 2005, in press.
[58] K.Koshino and T.Ogawa, J.Phys.Soc.Jpn. 68(1999)2164.
[59] O.Sakai,T.Ogawa and K.Koshino, J.Phys.Soc.Jpn. 71(2002) 978; O.Sakai,M.Ishii, T.Ogawa and K.Koshino, J.Phys.Soc.Jpn. 71 (2002) 2052.
[60] K.Matsuda, A.Machida, Y.Moritomo and A.Nakamura, Phys.Rev.B58(1998)R4203.
[61] E.Fortin, S.Fafard and A.Mysyrowics, Rhys.Rev.Lett.70 (1993)3951.
[62] T.Karasawa, H.Mino and M.Yamamoto, Journal of Luminescence 87-89(2000)174.
[63] T.Inagaki, T.Iida, M.Aihara, Phys.Rev.B 62 (2000)10852.
[64] S. Weinberg, The First Three Minutes, (Basic Books, 1993, New York).

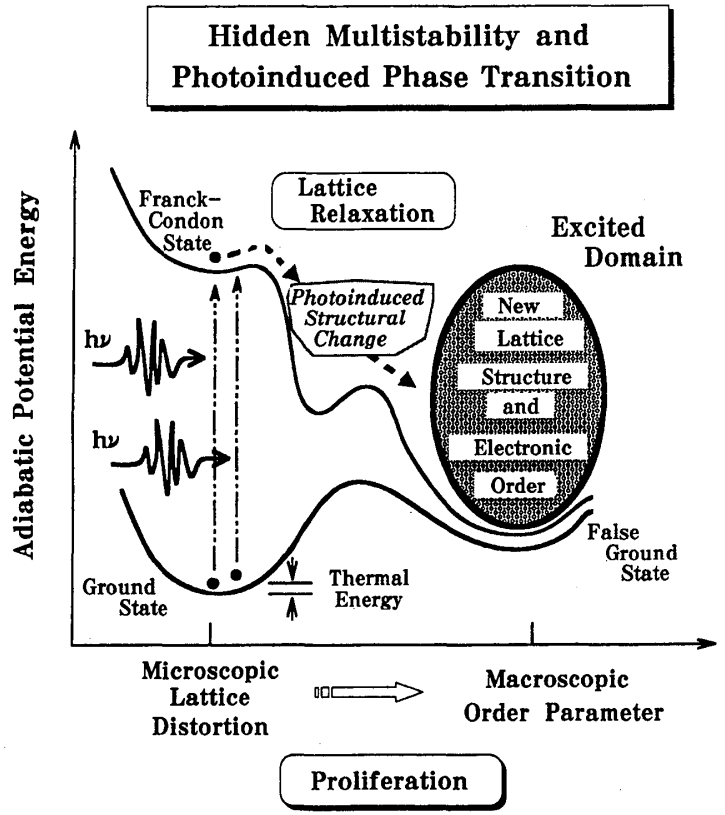

Fig.1 Schematic and conceptional natures of photoinduced structural phase transition, hidden multi-stability and proliferation.

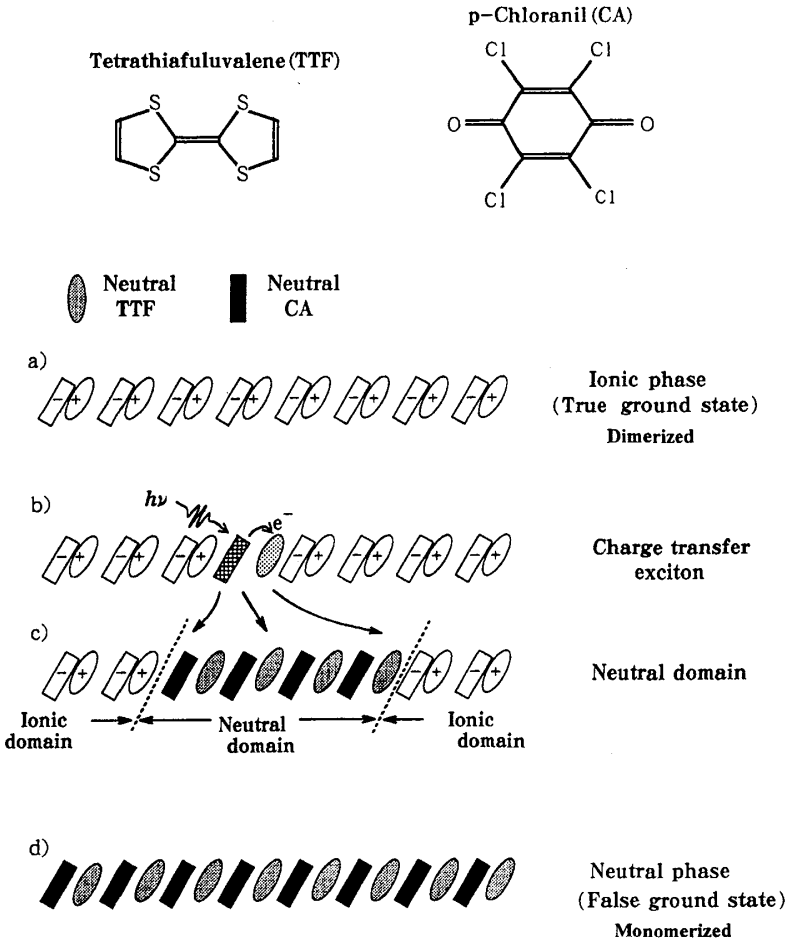

Fig.2 Schematic nature of photoinduced ionic→neutral structural phase transition in TTF-CA crystal. a) Ionic phase, b) Charge transfer exciton, c) Neutral domain, d) Neutral phase.

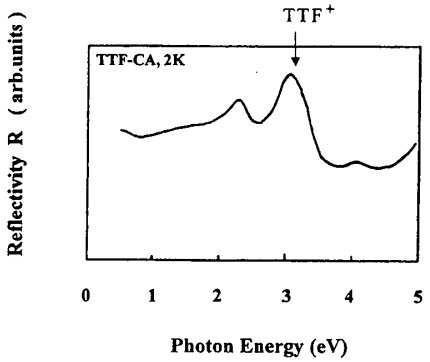

Fig.3. Spectral shape of original optical reflectivity (≡ R) of the TTF-CA crystal in the I-phase at 2K. The exciting light is polarized perpendicular to the 1-d chain axis. Peak at around 3eV corresponds to an intra-molecular electronic excitation of TTF^+. From ref. 7.

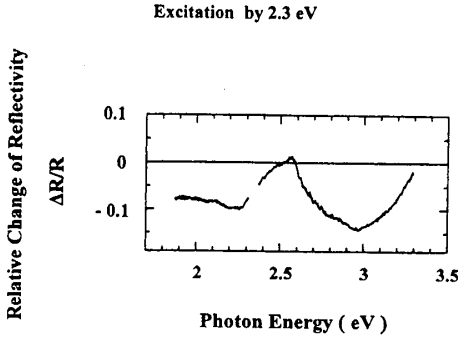

Fig.4 Relative change (≡ ΔR/R) of the reflectivity, when the TTF-CA crystal is shone by a light with an energy of 2.3eV. From ref.8.

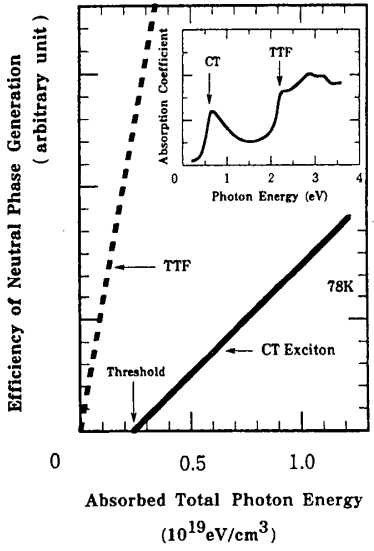

Fig.5 The efficiency of neutral phase generation in TTF-CA as functions of total absorbed photonic energy. The horizontal axis denotes the total photon energy absorbed in the unit volume of the TTF-CA crystal. This total energy is calculated by taking the three quantities into account: the absorption coefficient, the energy of the photon and its intensity. The thick solid line is the CT excitation (0.6eV), while the thick dashed line is the intra-molecular excitation (2.3eV). The small inset denotes the light absorption spectrum of TTF-CA crystal. From ref.9.

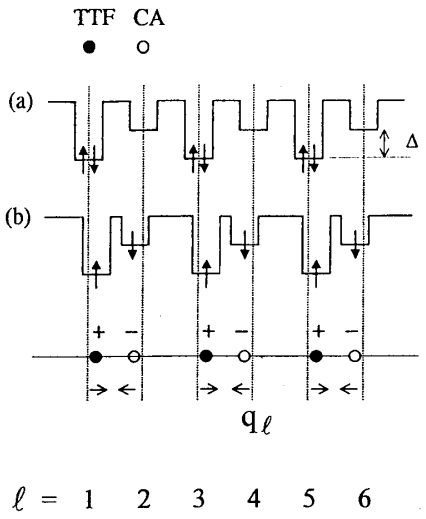

Fig.6 Schematic nature of neutral(a) and ionic(b) phases in TTF-CA crystal. Up and down arrows denote the electrons and their spins. Δ denotes the energy difference between the HOMO and the LUMO. q_λ is the displacement of the molecule at that site.

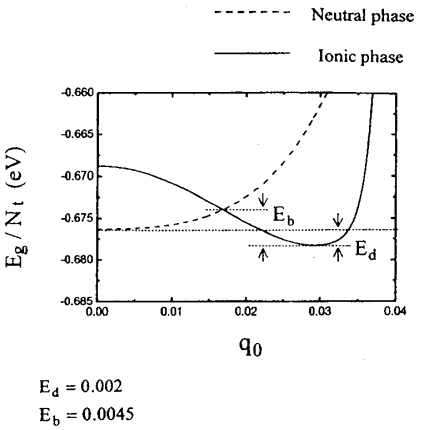

Fig.7 Total energy per site for ionic and neutral phases as functions of q_0. From ref.11.

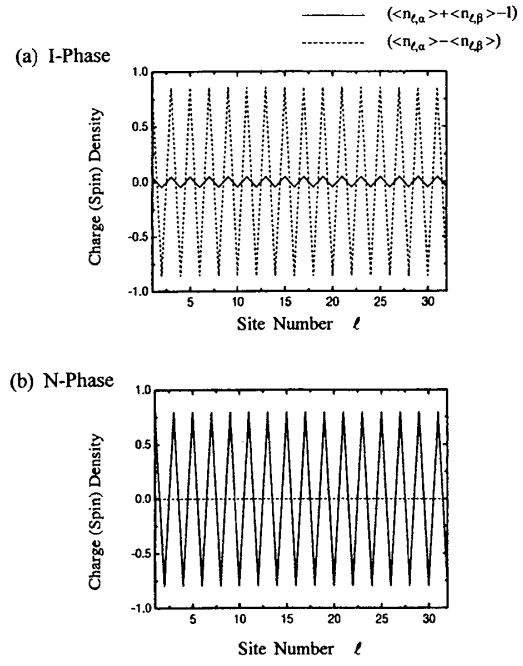

Fig.8 Charge and spin densities of ionic(a) and neutral(b) phases as functions of λ. From ref.11.

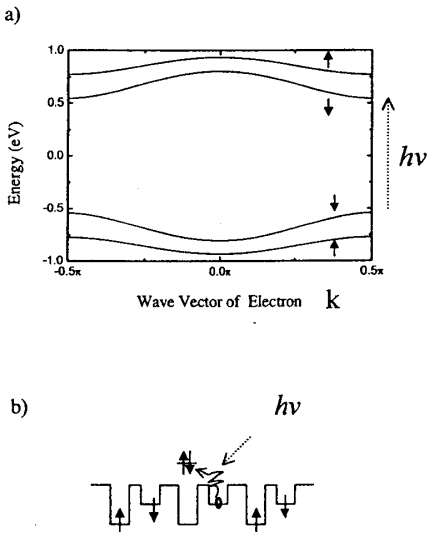

Fig.9 (a)The energy bands in the ionic phase. The lower wo bands are occupied by up and down electrons s denoted by corresponding arrows. The dashed line denotes the lowest excitation in the band picture. (b) Schematic nature of the charge transfer excitation in real space. From ref.11.

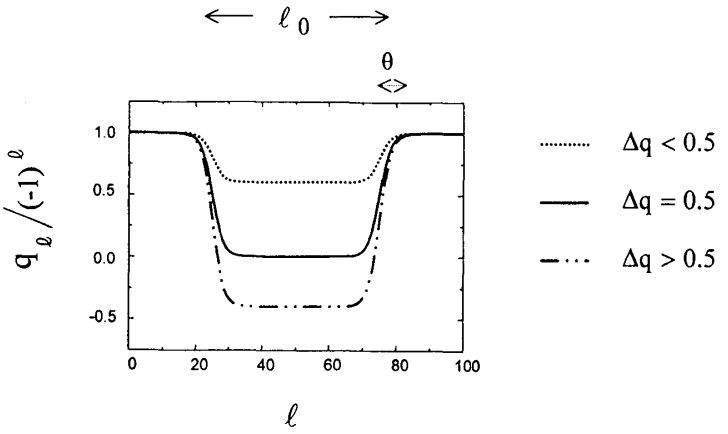

Fig.10 The domain type lattice distortion pattern to describe the relaxation, shown as functions of λ. Δq is its amplitude, θ corresponds to the width of the domain boundary, and λ_0 is the domain size.

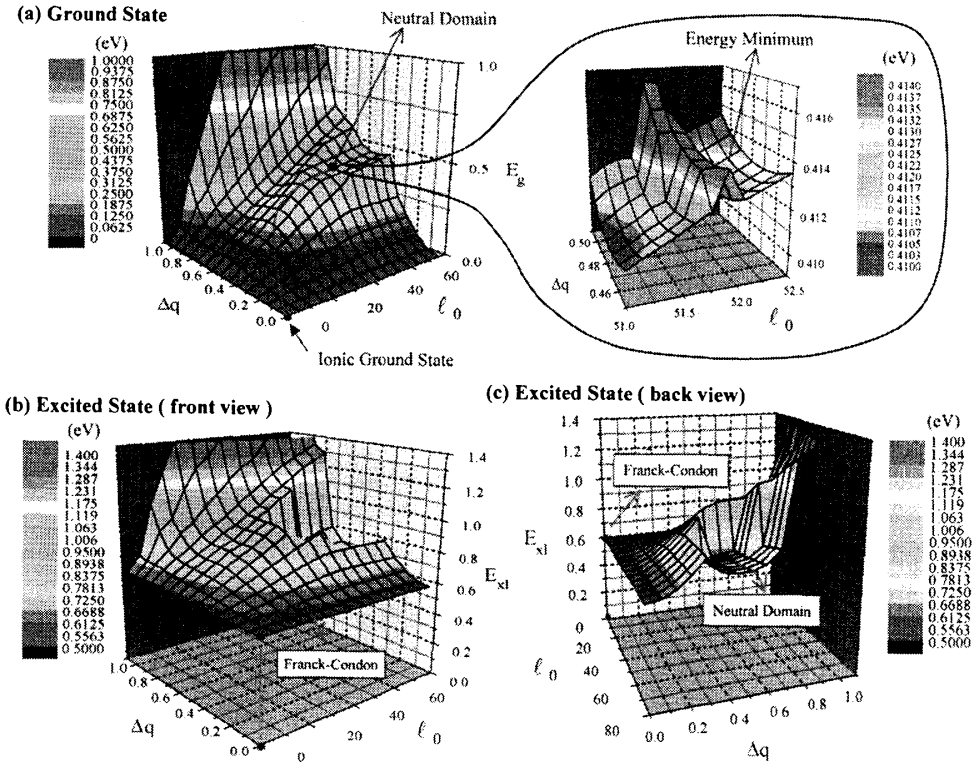

Fig.11 The calculated adiabatic energy surfaces in a two dimensional space spanned by Δq and λ_0. (a)The ground state E_g. The red line denotes the steepest ascending line from the ionic true ground state to the neutral domain. The enlarged inset denotes one of local energy minima. (b) The front view of the lowest excited state E_{x1}. (c) The back view of the lowest excited state E_{x1}. All the energies are referenced from the ionic true ground state. From ref.11.

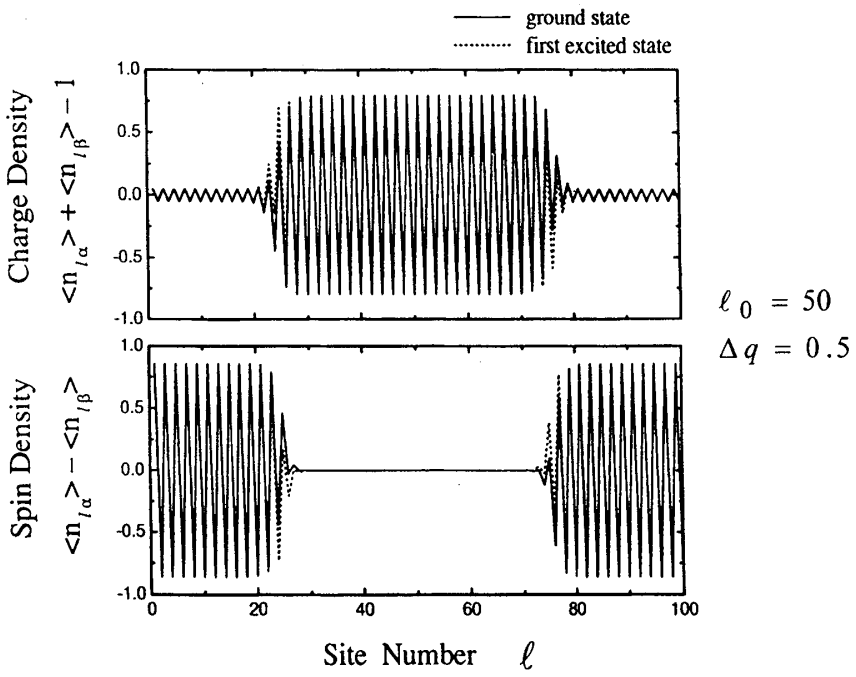

Fig.12 Charge- and spin-density distributions of the N-domain in the I-phase. Solid lines(ground state), dashed lines(lowest excited state). $\Delta q = 0.5$, $\lambda_0 = 50$. The original SDW type order inside of the domain has disappeared and a CDW type order has appeared instead. From ref.11.

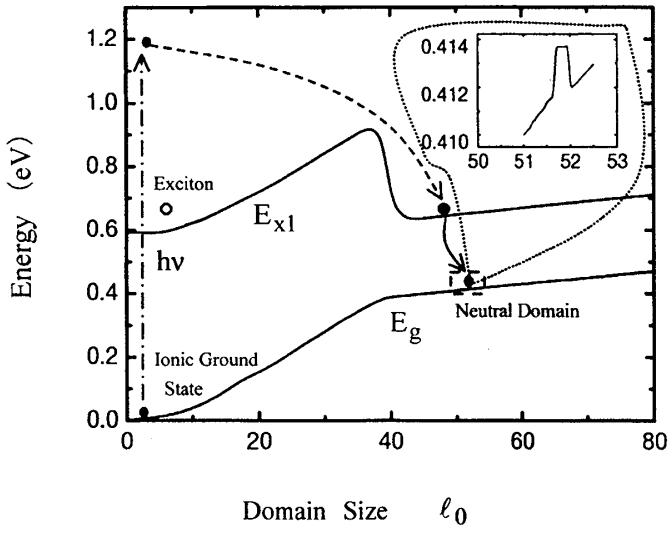

Fig.13 The adiabatic energies of the ground state E_g and the lowest excited state E_{x1} along the steepest ascending line shown by the red line in Fig.11. The dashed line denotes the expected relaxation path to generate the neutral domain. The enlarged inset denotes one of local minima. From ref.11.

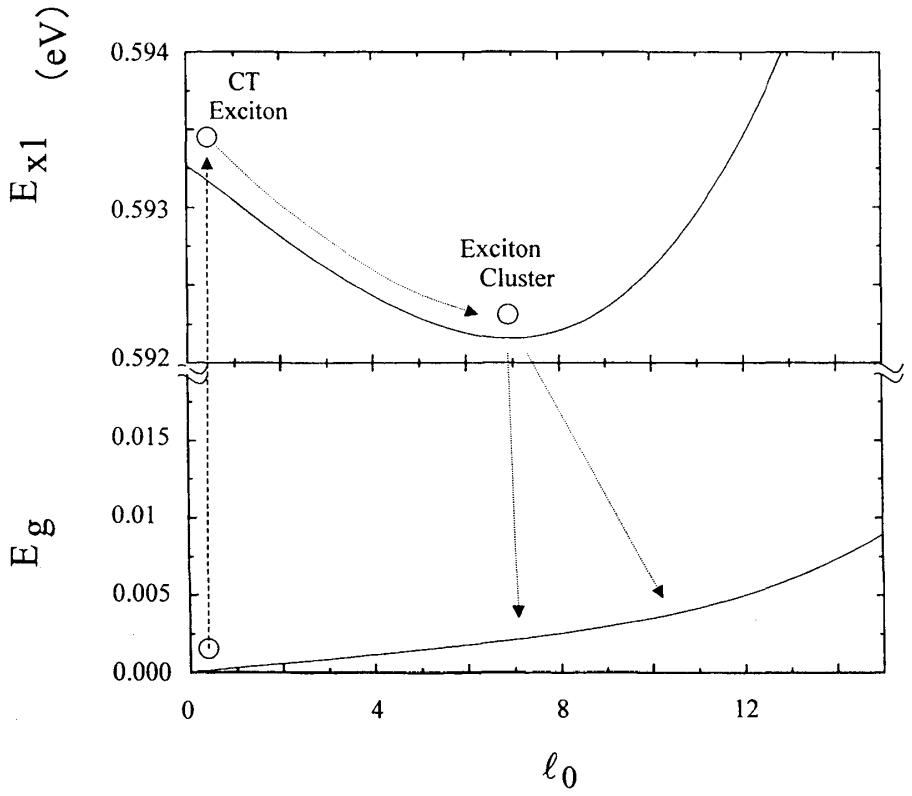

Fig.14 The adiabatic energies of the ground state E_g and the lowest excited state E_{x1} around the Franck-Condon region. The local energy minimum at $\lambda_0 \approx 7$ is a small CT exciton cluster. From ref.11.

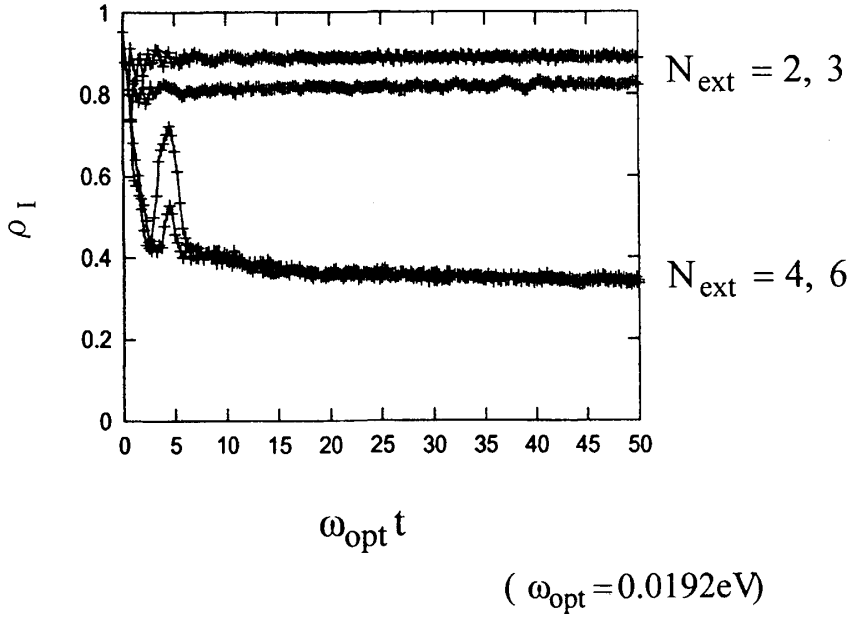

Fig.15 ρ_I as a function of real time t. From ref. 24. N_{ext} specifies the exciting time period, $0 < t < N_{ext}\, 2\pi/\omega_{ext}$.

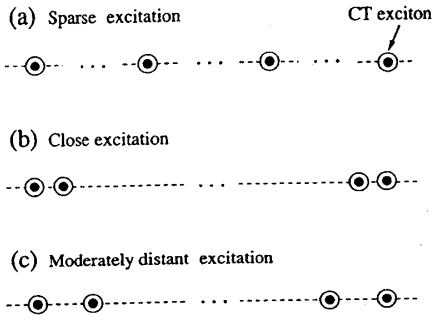

Fig.16 Schematic nature of CT exciton excitations with various distances. (a)Sparse, (b)close and (c)moderately distant excitations.

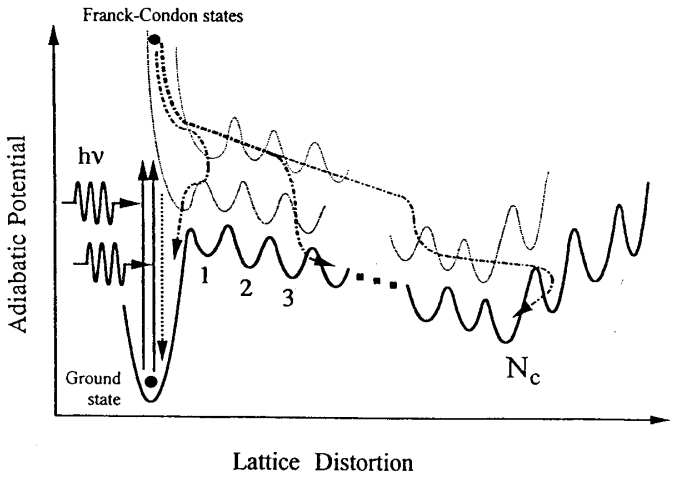

Fig.17 Schematic nature of the dynamics of exciton relaxation and the domain formation. The solid curve and thin dotted curves denote adiabatic potential surfaces of the ground and excited states. The global minimum of the lowest curve denotes the ground state. The other local minima 1, 2, ∧ of this curve denote the lowest energy states with 1, 2, ∧ excitons, respectively. The local minimum N_c has the lowest energy among these local minima 1, 2, ∧ . The upward solid arrows denote the initial photoexcitations. The dashed-and-dotted arrows denote the main relaxation paths. The downward dotted arrow denotes radiative decay of excitons.

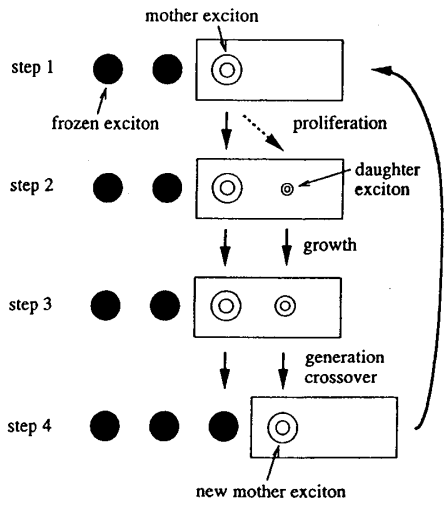

Fig.18 Schematic nature of the iterative equation, ∧ and the generation crossover.

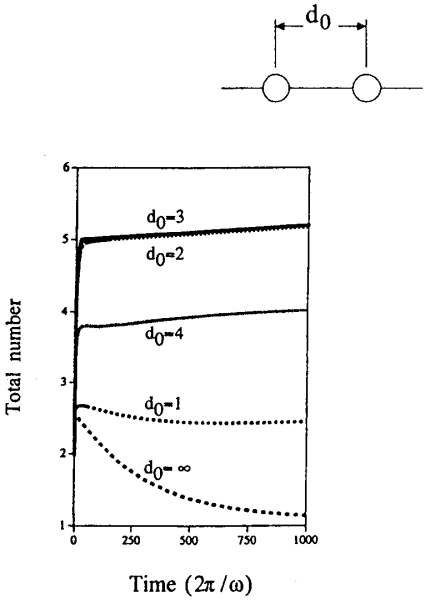

Fig.19 The total number of exciton as functions of time. d_0 is the distance between the initial two excitons. From ref.26.

$d_0 = 3$

G_e	t ($2\pi/\omega$)	Spatial Arrangement
1	0	○ ◉ ○ ○ ●
	1.1	0.44 0.53 0.48 0.56
2	1.1	○ ○ ◎ ○ ● ●
	2.8	0.31 0.57 0.56 0.54
3	2.8	○ ○ ● ◎ ○ ● ●
	2.3×10	0.00 0.09 0.98 0.92
4	2.3×10	○ ○ ○ ● ● ◎ ● ●
	4.6×10^3	0.13 0.30 0.57 1.00
5	4.6×10^3	○ ○ ○ ◎ ● ● ● ● ●
	9.0×10^3	0.13 0.31 0.57 0.99
6	9.0×10^3	○ ○ ○ ◎ ● ● ● ● ● ●
	1.3×10^4	0.10 0.31 0.60 0.99
7	1.3×10^4	○ ○ ○ ◎ ● ● ● ● ● ● ●
	1.9×10^4	0.17 0.26 0.59 0.99
8	1.9×10^4	○ ○ ○ ◎ ● ● ● ● ● ● ● ●
	2.1×10^4	0.01 0.37 0.63 0.99
9	2.1×10^4	○ ○ ○ ◎ ● ● ● ● ● ● ● ● ●

Fig.20 A spatial arrangement of excitons at the beginning of each generation(the step 1 in Fig.17). $d_0 = 3$.

G_e and t denote the generation and the time measured from the beginning of the first generation, respectively. The black circle and the double one denote a frozen exciton and a mother one, respectively. The white circle with a black one denotes the mother exciton created by the Franck-Condon excitation from the ground state. The values under each arrangement denote the exciton densities in the front, just before the generation crossover (the step 3 in Fig.17). The values of frozen exciton densities are almost equal to 1, and hence they are not written. From ref.26.

$$V_e(1) > 0,\ V_e(\sqrt{2}) < 0,\ V_e(1) > |V_e(\sqrt{2})|$$

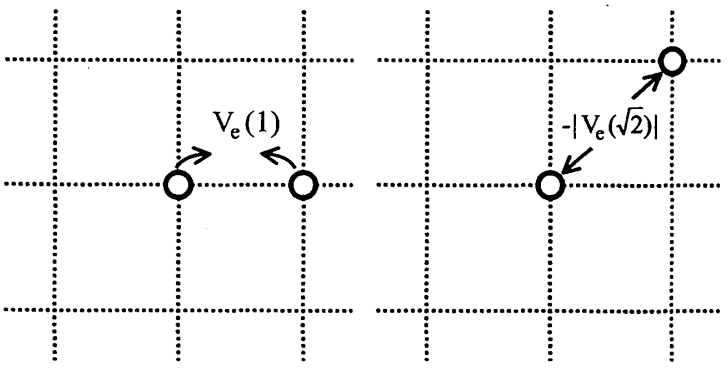

Fig.21 Anisotropy of inter-ecition interaction

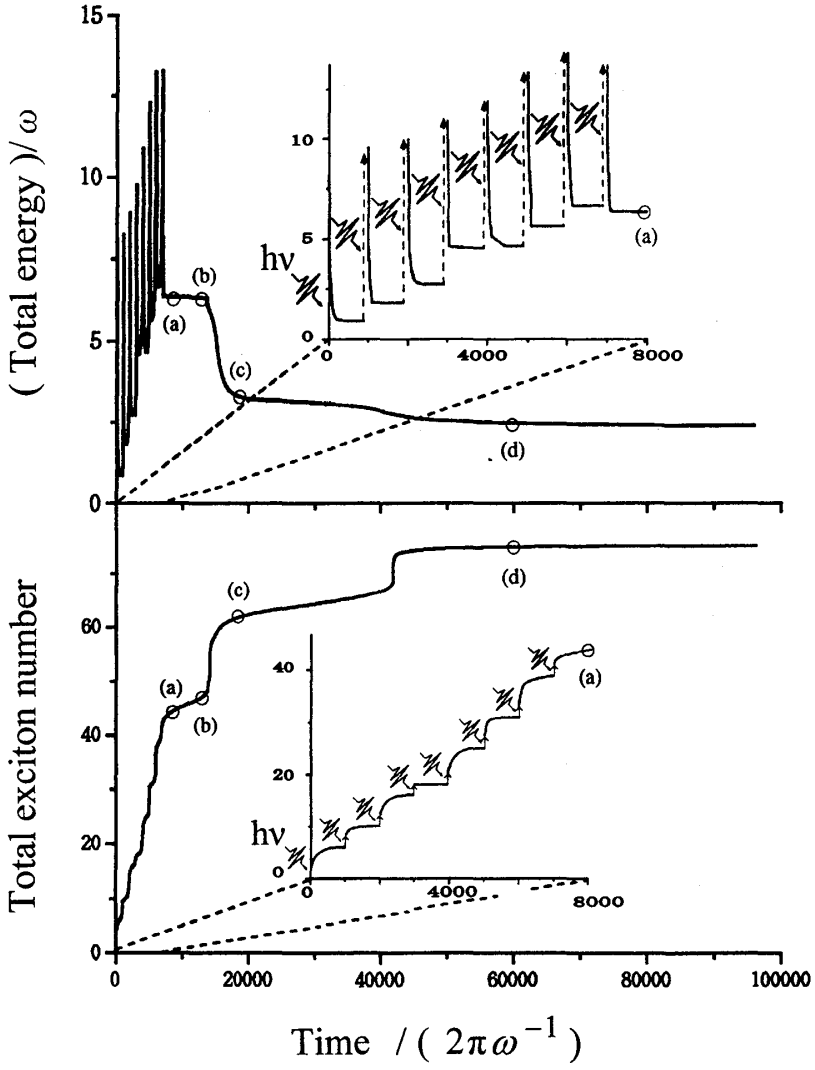

Fig.22 Total energy and total exciton number as functions of time. From ref.27.

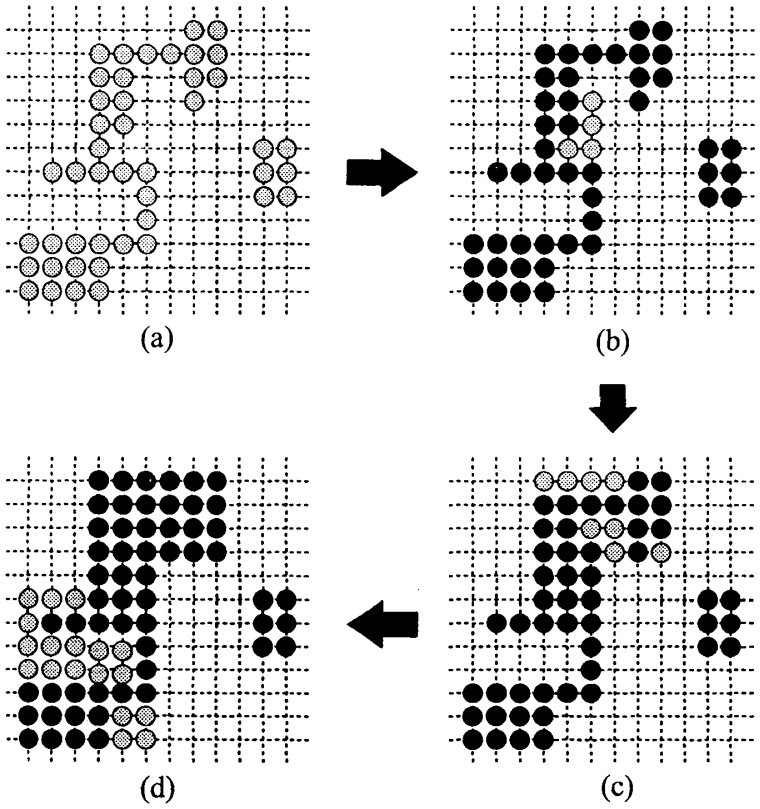

Fig.23 The spatial domain pattern. (a), (b),(c) and (d) are the time points shown in Fig.22. The gray circle is newly generated exciton. The black circle is the frozen exciton already generated until the previous time point. From ref.27.

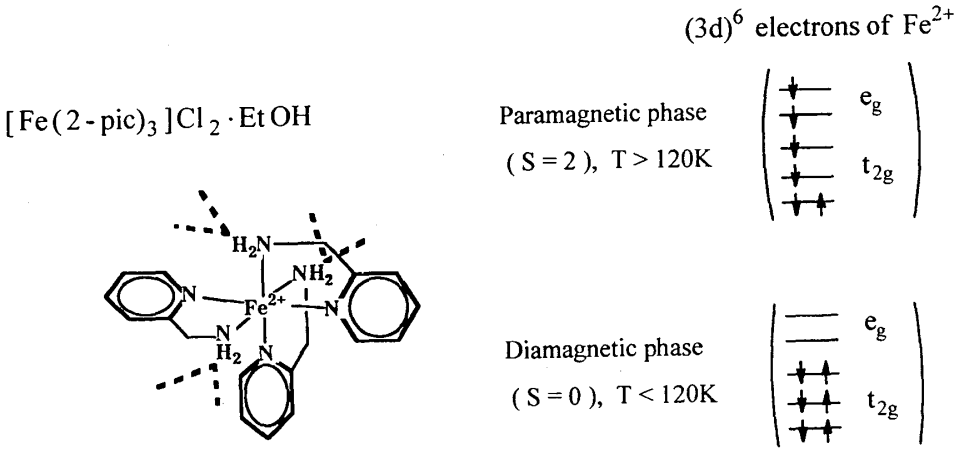

Fig.24 The structure and electronic states of $[Fe(2\text{-}pic)_3]Cl_2 \cdot EtOH$.

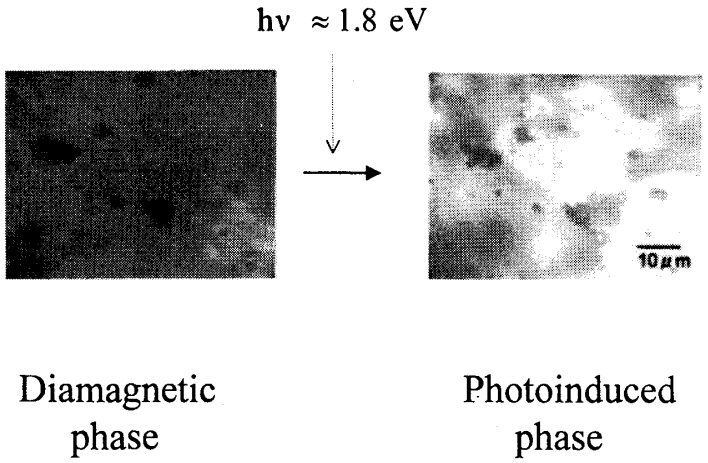

Fig.25 The photoinduced phase transition in $[Fe(2-pic)_3]Cl_2 \cdot Et\,OH$. From ref.30.

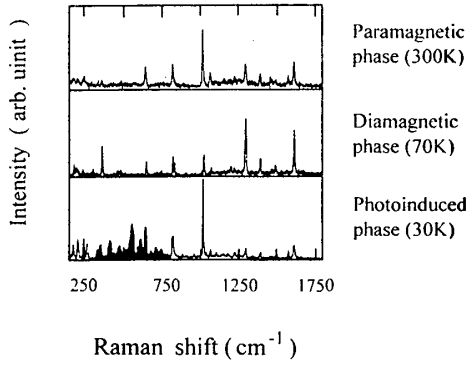

Fig.26 The Raman spectra of $[Fe(2-pic)_3]Cl_2 \cdot Et\,OH$, in the paramagnetic phase (300K), the diamagnetic phase (70K) and the photo-induced phase (30K). The shaded area of the photoinduced phase denotes the eccentric difference from other two spectra. From ref.31.

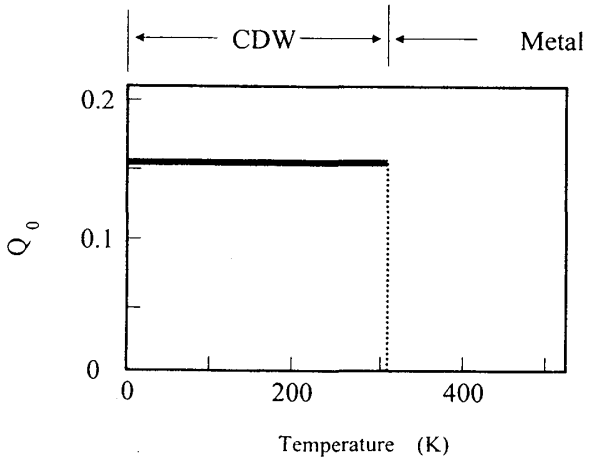

Fig.27 The phase diagram, and Q_0 as a function of temperature T. From ref.32.

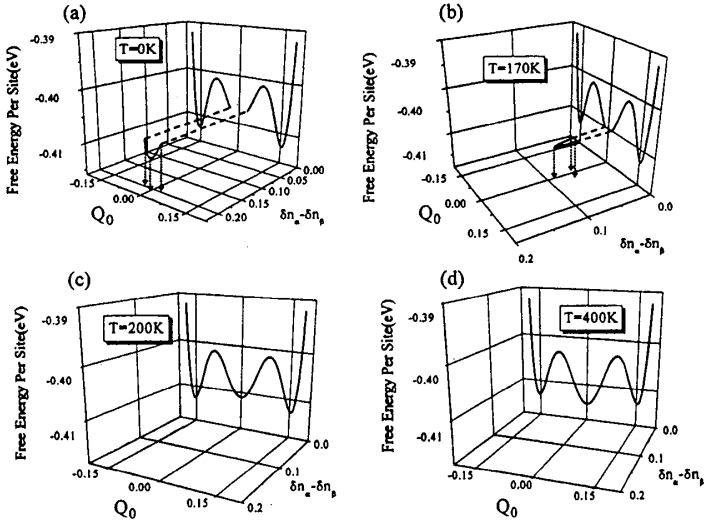

Fig.28 The free energy (per site) in the two-dimensional space spanned by the lattice distortion amplitude Q_0 and the SDW type order parameter ($\delta n_\alpha - \delta n_\beta$). (a)T=0K, (b)T=170K, (c)T=200K, (d)T=400K. From ref.32.

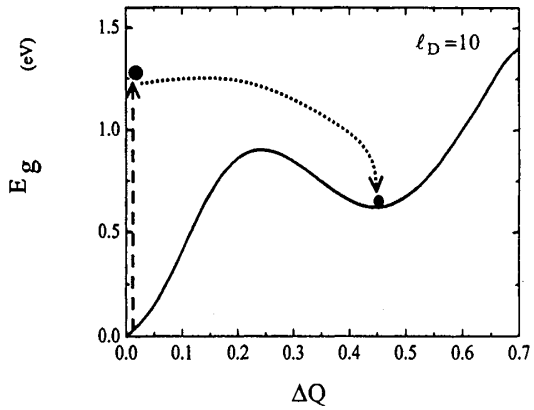

Fig.29 The adiabatic energy of the ground state E_g as a function of ΔQ. Energy is referenced from the true ground state. λ_D=10. From ref.32.

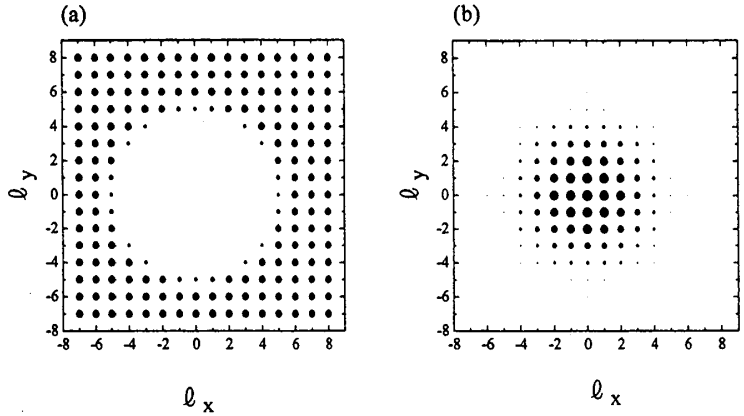

Fig.30 (a)The lattice distortion Q_λ of the domain. The diameter of dots are proportional to $|Q_\lambda/Q_0|$. (b) The spin density of the domain $<n_{\lambda\alpha}>-<n_{\lambda\beta}>$. The diameter of dots are proportional $|<n_{\lambda\alpha}>-<n_{\lambda\beta}>|$ at each lattice site. The value of $|<n_{\lambda\alpha}>-<n_{\lambda\beta}>|$ at the center of the domain is almost equal to that of Fig.24(a). From ref.32.

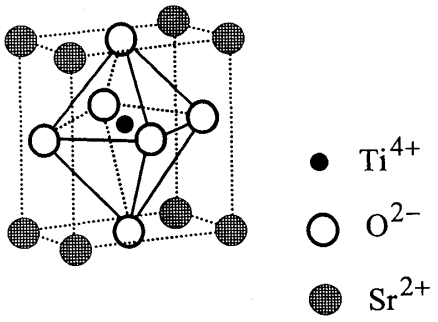

Fig.31 Schematic structure of $SrTiO_3$.

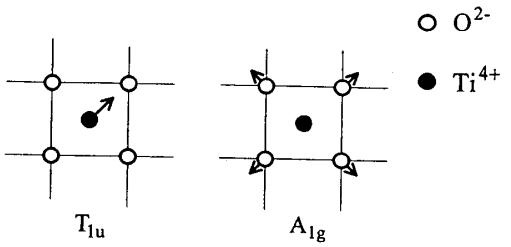

Fig.32 Schematic nature of T_{1u} and A_{1g} modes.

(a) $(\gamma s_d) = 0$

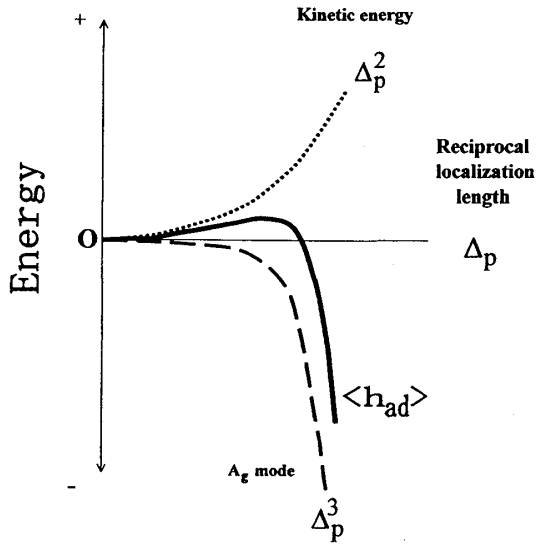

(b) $(\gamma s_d) \neq 0$

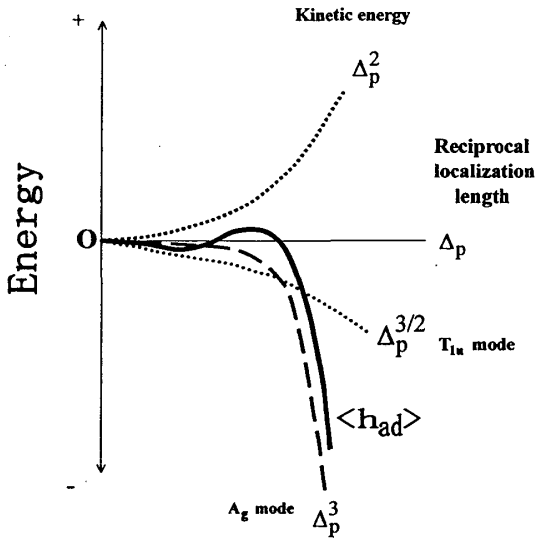

Fig.33 Schematic energetics of the self-trapping. (a) Without T_{1u} mode.
(b) With T_{1u} mode.

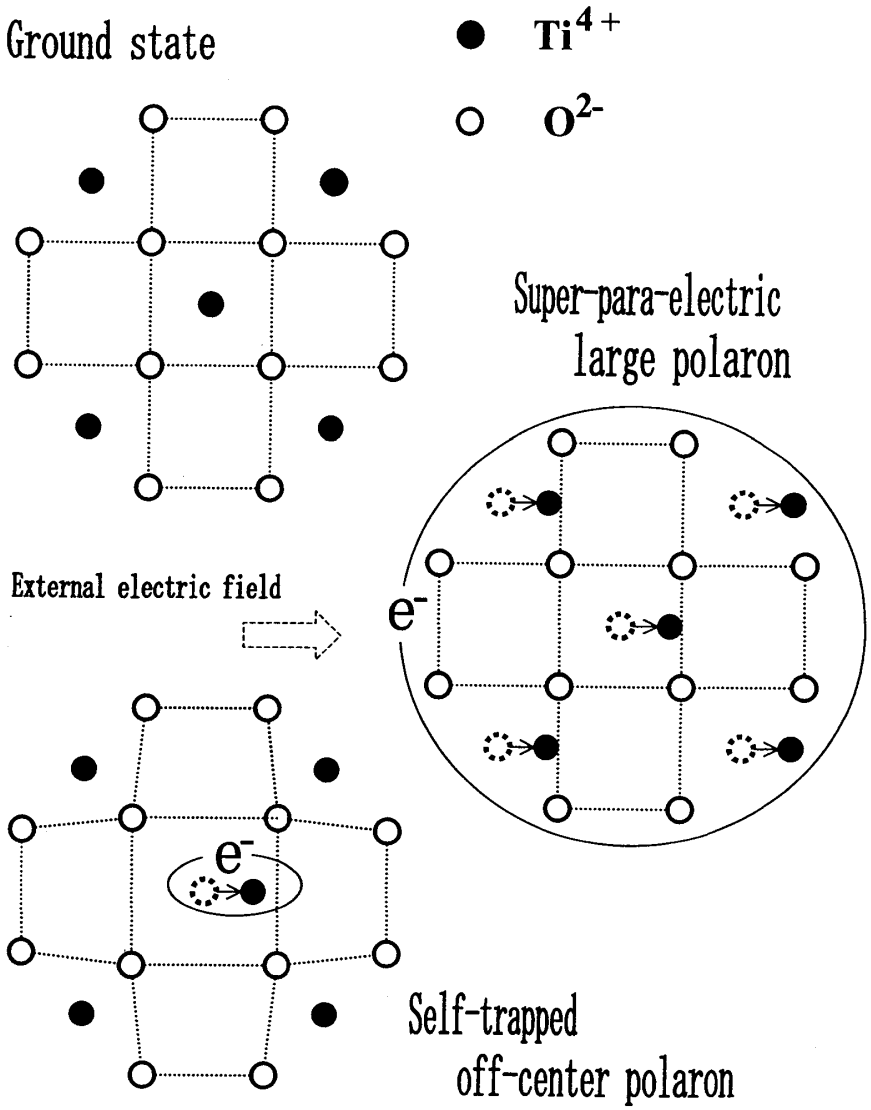

Fig.34 Schematic natures of the ground state, the super-pare-electric large polaron, and the off-center type self-trapped polaron.

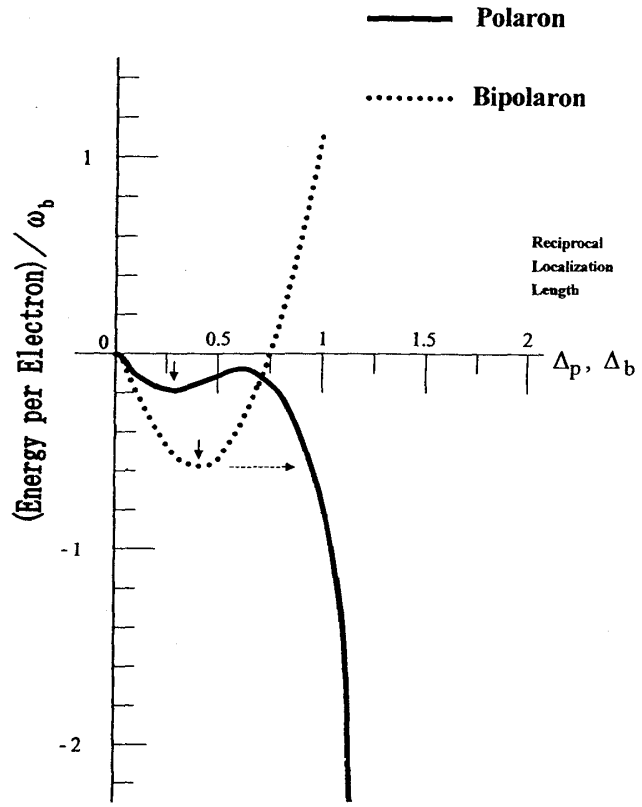

Fig.35 (Energy per electron)/ω_b of poaron and bipolaron, as functions of Δ_p and Δ_b. t=8.33, $s_b=200$, $\gamma=0.05$, $\gamma s_d=15$, $u/s_b=1.75$. From ref.36.

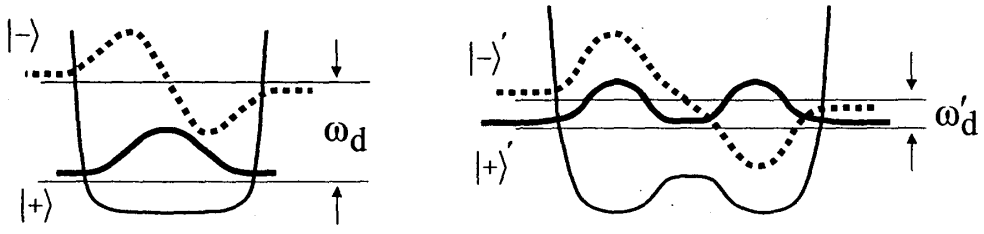

Fig.36 The lowest two vibronic states of the T_{1u} mode. (a) At the electronic ground state. (b) At the central lattice site of the super-pare-electric large polaron. ω_b=20meV, t=8.33, $s_b=200$, $\gamma=0.05$, $\gamma s_d=15$, $u/s_b=1.75$.